Collimating relativistic MHD jets from black hole accretion disks

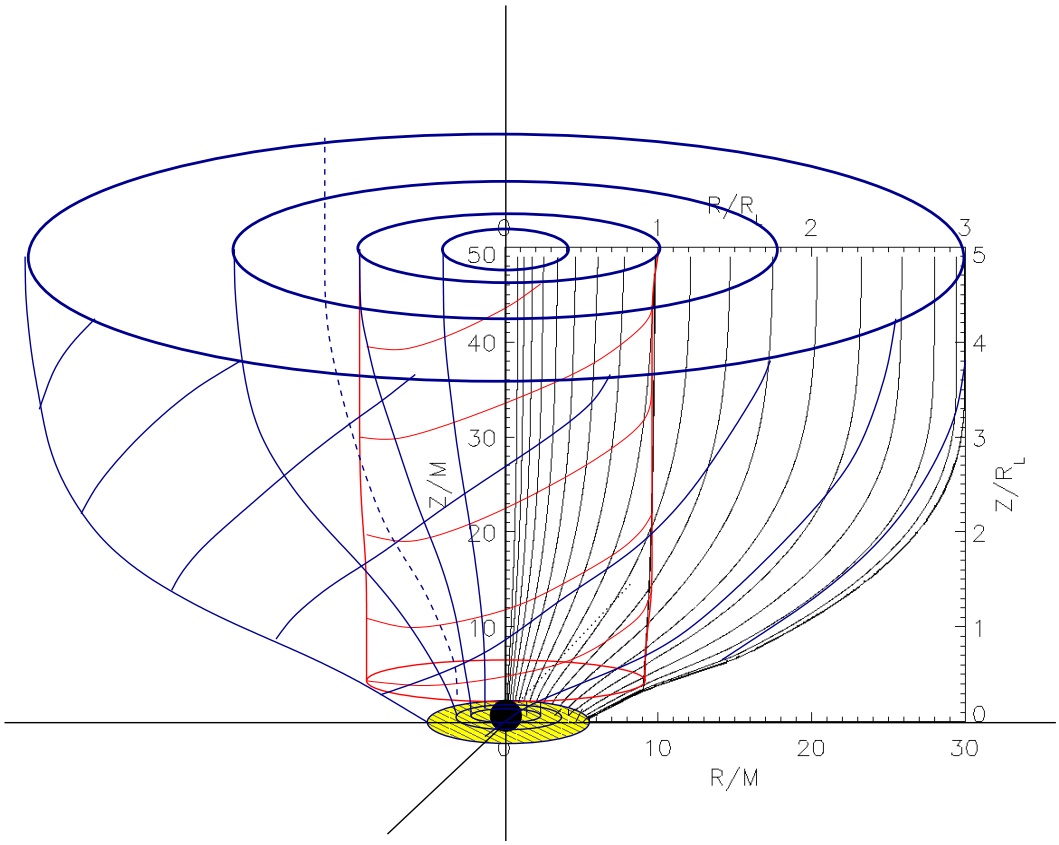

Master thesis by:
Sander von Benda-Beckmann (Leiden Observatory, Leiden)

Supervisors:
Dr. C. Fendt (AIP, Potsdam)
Prof. Dr. V. Icke (Leiden Observatory, Leiden)

Contents

1 Introduction **3**
- 1.1 Observations . . . 3
- 1.2 From observations to theory . . . 7
- 1.3 Review on models of (relativistic) MHD jets . . . 8
- 1.4 Topic of this thesis . . . 12

2 Magnetohydrodynamic Jets **14**
- 2.1 Model assumptions . . . 14
- 2.2 Grad-Shafranov Equation (GSE) . . . 18
  - 2.2.1 Normalizing the GSE . . . 23

3 Solving the Grad Shafranov Equation **25**
- 3.1 Regularity condition at the light surface . . . 25
- 3.2 Boundary condition at the jet axis . . . 26
- 3.3 Jet surface boundary condition . . . 26
- 3.4 Disk and black hole boundary conditions . . . 27
- 3.5 Asymptotic solution for the special relativistic GSE . . . 28
  - 3.5.1 Free functions $\Omega_F(x)$ and $I(x)$ of the GSE . . . 30
  - 3.5.2 The asymptotic light surface . . . 32
  - 3.5.3 Solving the asymptotic GSE . . . 34
  - 3.5.4 Scaling the 2-D solution to the central mass of the black hole . . . 35
- 3.6 Grid boundaries . . . 40
  - 3.6.1 Light surface . . . 40
  - 3.6.2 Outer jet surface . . . 42
  - 3.6.3 Disk & black hole boundaries . . . 43
  - 3.6.4 Summary of the jet-model . . . 44

4 Code Development/Testing **47**
4.1 Developing the code 47
4.2 Testing the code 50
4.2.1 Constant rotation 51
4.2.2 Differential rotation 55

5 Discussion & Future Work **60**
5.1 Discussion 60
5.2 Calculating the flux structure from disk physics 64
5.3 Solving the energy equation along the flux surfaces 67
5.4 Polarization of the jet synchrotron emission 69

6 Conclusion **72**

Chapter 1

Introduction

1.1 Observations

The phenomenon of highly collimated plasma streams with high velocities, called jets, has been observed amongst a variety of objects on wide scales in energies and spatial extensions. The most energetic and largest jets emerge from the nuclei of active galaxies (AGN) (e. g. Baade & Minkowski 1954; Zensus et al. 1995). Smaller jets with lower velocities have been observed around Young Stellar Objects (YSO) (e. g. Mundt & Friedt 1983; Mundt & Eislöffel 1998) and recently also around micro-quasars (MQ), what are thought to be high-mass X-ray binaries (e. g. Mirabel & Rodriguez 1999). There are also reasons to believe that Gamma-Ray Burst (GRB) might be a consequence of a jet-like source (for a recent review Mészáros 2002). Typical for jets is that they extend to huge distances away from the central object (with radii up to 1000 times the size of the central object), with the largest that can extend to up to 100 kiloparsecs.

Evidence for a central black hole in the nucleus of the E0 elliptical M87, that contains one of the nearest extra-galactic jets (at 14.7 Mpc) and is located at the center of the Virgo cluster, was found by Ford et al. (1994). Using HST spectroscopy of its nucleus, strong evidence was found for a rapidly rotating ionized gas disk at its center from which a mass for the central black hole was inferred of 3×10^9 M_{sun}. Also Kepler rotation for a cool thin disk around a black hole is found using VLBI maser emission in region between 0.13 and 0.26 pc in the NGC4258 galaxy that also contains a jet (Myoshi at al. 1995). In the case of micro-quasar GRS 1915 evidence has been found for

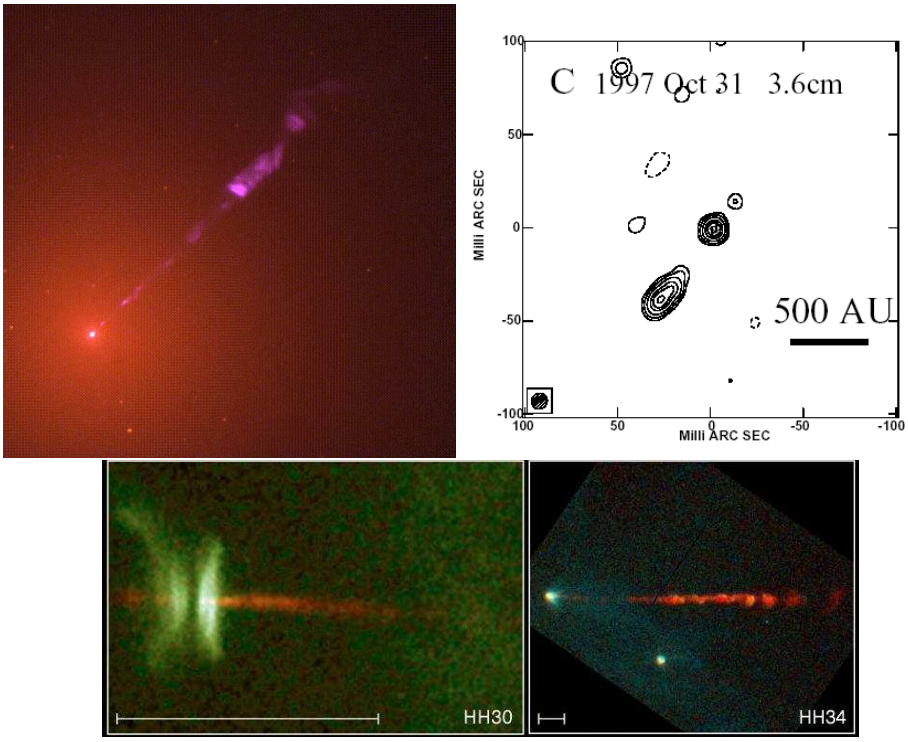

Figure 1.1: Top left: Optical image of the jet in the M87 elliptical galaxy. Top right: VLBA radio image of the micro-quasar PKS1915 (Dhawan, Mirabel & Rodríguez 2000). Bottom: HST images of protostellar jets around Young Stellar Objects (scale represents 1000 AU).

a central black hole with a mass of about 14 M_{sun} (Greiner et al. 2001). The apparent correlation of jet-activity with the presence of an accretion disk onto a central black hole has led to the general belief that the accretion disk and the black hole play an important part in the production process of these jets.

The M87 jet has been observed extensively at different wavelengths (VLA radio, HST optical/uv), has strong collimation ($\approx 6^o$), and extends to large ranges (100 kpc). Because it is relatively close and is strong it is an ideal jet to test models on jet formation. Junor et al. (1999) and Biretta et al. (2002) showed that the collimation of the M87 jet occurs in an area < 30 R_S (where R_S is the Schwarzschild radius) to the fully collimated zone > 100 R_S. For the black hole mass of M87 the R_S corresponds to about 0.0003 pc. The

measured opening angles for the jet as can be seen in Fig. 1.2 show that the jet collimates from an opening angle of $\approx 60^o$ to $\approx 6^o$. Their radio interferometry observations give the most detailed view yet on the collimating region of a jet.

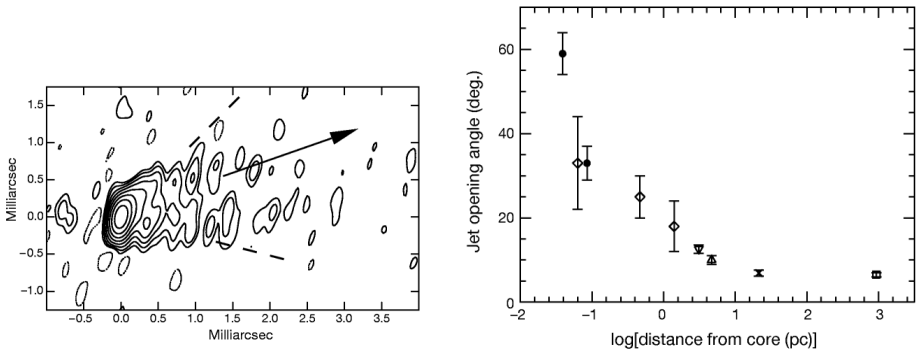

Figure 1.2: Radio observations of the collimation regime in the M87 jet (taken from Junor et al. 1999). On the left: The radio structure of the collimating jet in the core of M87. On the right: The jet opening angle at different distances from the jet core. This shows clearly the collimation of a wide wind into a narrow jet.

The question whether the jets content consists of electron-positron pairs, or electron-proton pairs has not been answered yet. Celotti & Fabian (1993) have addressed the issue of content of a sample of radio-loud quasars. They suggest that for the sample as a whole, either the flows are cold electron-positron flows or electron-proton flows with an energy cut-off of ≈ 50 MeV. Observations of the M87 jet by Reynolds et al. (1996) indicate that the M87 jet is likely to be an electron-positron dominated jet, based on standard synchrotron self-absorption theory. The question remains, however, whether based on a small sample of jets, a claim can be made over the matter content of jets in general.

There are many indications that magnetic fields are present within the jet. The most obvious is the synchrotron emission. Perlman et al. (1999; 2002) have done extensive research synchrotron emission, and polarization of the M87 jet. They report high polarizations that suggest highly ordered magnetic fields. Herrnstein et al. (1998) found for the disk in NGC4258 an upper limit for the magnetic field strength in the toroidal component of $B_T \leq$ 300 mG.

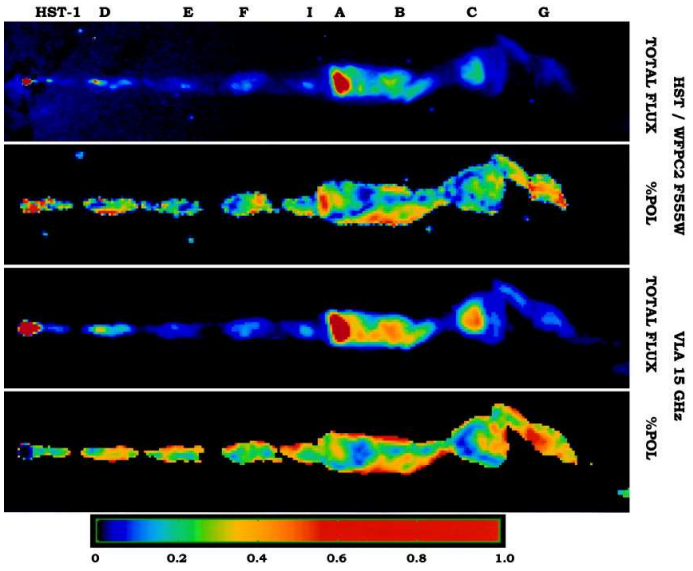

Figure 1.3: Polarization measurements of the M87 jet in the radio (lower) and optical (upper), taken from Perlman et al. (1999). The two false-color representations shows the total flux and the total degree of polarization for the optical and the radio emission.

Super-luminal motions of $3c-6c$ have also been observed in the case of jet ejected by AGN (for M87 by Biretta et al. 1999) and also by micro-quasars (Mirabel & Rodriguez 1999). This super-luminal motion is the result of a projection effect: When matter moves with velocities close to the speed of light in the direction of the observer, a transverse apparent velocity can be observed that exceeds that of light. The fact that these type of jets have these very high velocities distinguishes them from their low-velocity counterparts around YSOs. If the super-luminal motion observed is interpreted as the plasma motion itself, this implies high β-factors, which needs a relativistic treatment of the jet structure. These high velocities imply for a hydromagnetically driven jet, that the poloidal electric fields will play a relevant role in the force-balance, ($E_P \propto \beta B_P$), which is a relativistic effect. Therefore a relativistic treatment of these jets is inherently different from a Newtonian treatment.

1.2 From observations to theory

Many efforts have been made to explain the origin of these jets. Initially a mechanism to collimate the jet by gas pressure was suggested by Blandford & Rees (1974). They proposed that external gas pressure could create a 'de Laval nozzle' through which hot gas might be channeled outwards into a supersonic flow. The high pressures needed to obtain this collimation on a very small scale would cool rapidly, and should be observable. This has not been observed, so its absence would rule out this model (Krolik 1999). Although radiation forces could drive a wind, once one gets to mildly relativistic speeds, a medley of effects make further acceleration by a directed component of radiation extremely inefficient (Phinney 1987; Icke 1989). Blandford & Payne (1982) proposed a mechanism to eject matter from the disk into its magnetosphere. When gas is in balance between gravitation and centrifugal forces when poloidal magnetic fields are present, this leaves the possibility for a magneto-centrifugal instability. If the disk is magnetized, and has a poloidal magnetic field that makes an angle $< 60^{o}$ from the disk plane, (see Fig. 1.4) Blandford & Payne (1982) found that the gas may slide along the field lines away from the disk equator and then becomes centrifugally dominated leading to acceleration of the gas away from the central object. This mechanism is not only a possible mechanism of the initial acceleration of the gas, it also is a mechanism to remove angular momentum of the accretion disk, allowing it to accrete onto the central object. In order to describe these outflows, a hydromagnetic description is required. The magnetic fields observed (see Section 1.1) in the jets also provide good support for this idea. Although their presence does not necessarily imply their dynamics relevance in the jet, the fact that they theory needs them for the jet inititation and acceleration and that are observed does give a good argument for the hydromagnetic character of the jets.

The model that has emerged from these observations and has become widely accepted, is as follows: A central object (YSO, black hole) is surrounded by a magnetized accretion disk (see Fig. 1.5). Matter is lifted from the disk into the magneto-sphere and accelerated along the field lines. The initial wind then collimates into the jet, either due to self-collimation or to the ambient gas pressure. There are a lot of open questions still: How to collimate and accelerate a low-velocity wind into a high-velocity collimated jet? How to lift the matter from the disk into the magneto-sphere? How is the magnetic field generated inside the disk, or is it the field of the central

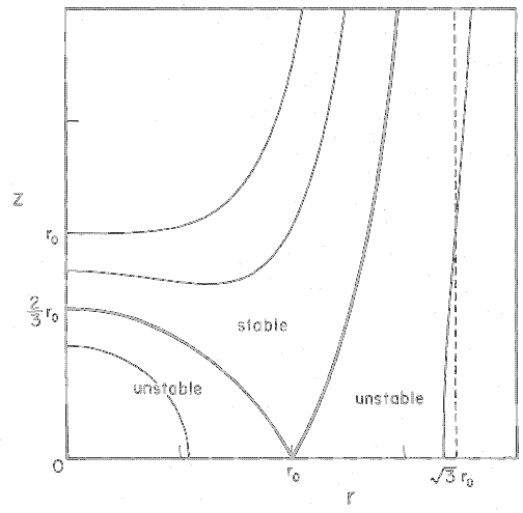

Figure 1.4: Equipotential surfaces for a 'bead on a wire' (plasma along magnetic field line), corotating with the Keplerian angular velocity at a radius r_0, which is released from rest at r_0. The equation for the surfaces is $\phi(r,x) = -\frac{GM}{r_0}[1/2\left(\frac{r}{r_0}\right)^2 + \frac{r_0}{(r^2+z^2)^{1/2}}]$ = constant. These surfaces are equal intervals of $\phi(r,z)$. If the wire makes an angle of less than 60^o with the equatorial plane, the equilibrium is unstable (taken from Blandford & Payne 1982).

object? How stable is a hydro-magnetic driven jet? In this thesis I will focus on the first question. Before presenting the work that I have done for my graduation project with Christian Fendt (AIP, Potsdam), I first give a brief review on the work that has been done in the field.

1.3 Review on models of (relativistic) MHD jets

There has been done a great amount work of modeling (relativistic) jets. A brief overview will be given here of the different approaches which have been used.

The types of studies that have been done can be divided broadly into stationary and time-dependent studies. An approach to fully self-consistently describe the initial formation and then the collimation, propagation and sta-

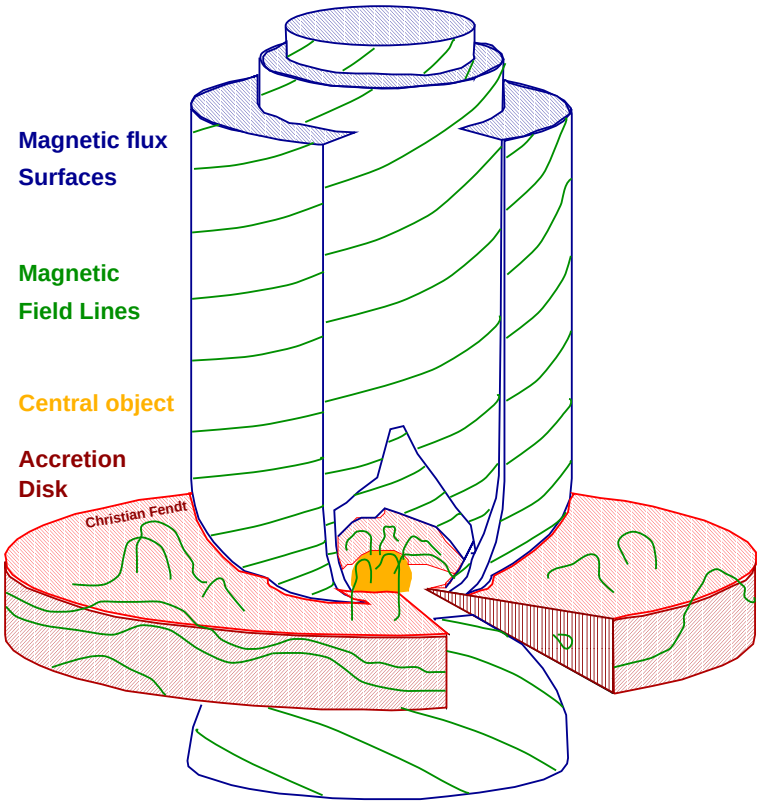

Figure 1.5: A schematic model for the jet structure: A central object, surrounded by a magnetized accretion disk. The gas lifts from the disk and moves along the poloidal magnetic field lines and collimated into a narrow jet.

bility of the jets would of course need a time-dependent model. The regions from the initial wind formation out to the collimated jet structure spans an enormous spatial range, what makes it difficult, even nowadays, to solve this complicated and time consuming problem. Because these problems have to be solved numerically and due to the lack of computational power only small regions above the disk can be simulated and typical time-scales of these simulations only span up to one rotation of the outer part of the disks, which is too little in order to address the stability of the jet formation process. In order to study the jet on global scales the problem is often simplified, based on reasonable argumentation, by assuming the jet to be stationary. Because this assumption is made for the work presented in this thesis I will mainly

give a review narrowed down on the stationary models.

Stationary models The research done on stationary hydro-magnetic driven jets has been concerned mainly with considering the cross-field force balance, known as the Grad-Shafranov Equation (GSE), and the Wind-Equation (also known as the Bernoulli Equation), that describes the energy conservation along the flow lines.

Blandford & Payne (1982) started out with the assumption that the geometry of the jet was *self-similar*. This could be used to reduce the complicated GSE into a set of ordinary differential equations. Self-similarity can be motivated by assuming a power-law distribution for various physical quantities (gas density, pressure, and magnetic field distribution). In the case of a Keplerian disk, this holds quite well close to the disk surface. Their approach was extended by Li et al. (1992) for relativistic jets. A general result of the self-similar approach is that the jet tends to re-collimate in the case of high fast-magnetosonic Mach numbers. This has been proven to be an artifact of the self-similar assumption (Ferreira 1997). Pelletier & Pudritz (1992) dropped the self-similar Ansatz and took into account the gas pressure. Although their solutions were two-dimensional, the regimes below the slow-magnetosonic point and the region beyond were treated separately.

Another self-consistent approach to solve the GSE was conducted by Li (1993). By starting with an initial flux-field distribution at the base of the jet, a set of flux fields was constructed by considering locally the force-balance and conserving the conserved quantities: the mass flow along the flux surfaces $\eta(\Psi)$, the total energy $E(\Psi)$ and the angular momentum per unit density $L(\Psi)$.

Lovelace et al. (1991, 1993) proposed a parameterization of the cylindrical radius in terms of the jet radius, which was chosen together with separation of variables. This, however, did not consider the local-force balance described by the GSE. Contopoulos & Lovelace (1994) returned to the self-similar Ansatz and presented an exact solution by considering the local force-balance. Contopoulos (1995) also proposed an alternative driving mechanism for jets, in absence of large poloidal fields. In this case the magneto-centrifugal mechanism by Blandford & Payne does not work, and the matter then can be accelerated by the pressure gradient of strong toroidal fields provided by the accretion disk.

Heyvaerts & Norman (1989) derived analytically that axisymmetric MHD

flows enclosing a net poloidal current will collimate to a cylindrical shape in the asymptotic region far away from the flow origin. This has been proved later in the case of relativistic jets as well by Chiueh et al. (1991). The resulting one-dimensional version of the GSE has been studied by Appl & Camenzind (1993). Instead of a self-similar approach, they assumed the flow to be *force-free*, i. e. the electromagnetic forces dominate the inertial forces. They found that the jet structure could be characterized by a core-radius, and that most of the magnetic flux and electric current lies within this core radius. This approach was extended by Fendt (1997) for differential rotation of the flux surfaces. It was found that jets with differential rotating flux-surfaces will have narrower jets in terms of the asymptotic light cylinder (see Section 2.2).

Okamoto (1992) investigated the possibility of energy and angular momentum extraction from a force-free black hole magnetosphere due to a wind. He derived an analytical expression that couples the the poloidal current $I(\Psi)$ and the field rotation $\Omega_F(\Psi)$. This work was based on the idea Blandford & Znajek (1977) proposed, that force-free magnetic fields coupled to a fast rotating black hole may lead to extraction of energy and angular momentum by a pure electro-magnetic process (Blandford-Znajek mechanism). The most general treatment (but not full solutions) of the GSE including inertial terms close to a black hole has been done Nitta et al. (1991) and Beskin & Pariev (1993). Takahashi et al. (1990) obtained solutions of the Wind-Equation in Kerr metric, mainly discussing the accretion flow. This has been extended by Fendt & Greiner (2001) discussing the leading parameters of Kerr metric a and M on the flow acceleration.

Two-dimensional stationary models Two-dimensional solutions for the GSE have been calculated by amongst others Sakurai (1985). These were non-relativistic solutions including inertial terms, but for a slow-rotating star (initial radial outflow, Sakurai 1985) and disk (split-monopole like initial configuration, Sakurai 1987). These, however, show a low degree of collimation, mainly due to the slow rotation. For relativistic force-free MHD winds, Camenzind (1986,1987) developed a method, based on a finite elements approach, in order to solve the axisymmetric GSE. Although the solutions were two-dimensional, the regularity condition at the light surface were not treated correctly. These were extended by Fendt et al. (1995, 1997) to calculate the global solution for highly magnetized stars (Fendt et al. 1995)

and for rotating black holes (Fendt 1997). Also the regularity condition was treated properly. Fendt & Memola (2001) included, in a special relativistic approach, the differential rotation terms of the flux-fields. Bogovalov (1997) has obtained stationary solution for a relativistic MHD wind, by solving the time-dependent problem. Also he finds solutions with only weak collimation. Recently Heyvaerts & Norman (2003) presented a general and global solution for non-relativistic MHD jets and winds including inertial terms (a polytropic gas pressure was assumed). Here also the return current is taken into account. They found that for winds, where the kinetic energy dominates at infinity, the magnetic surfaces focus into exponential paraboloids and for a Poynting flux dominated wind, the surfaces collimate into nested cylindrical surfaces. Their approach takes only constant rotation of the flux-surfaces into account.

1.4 Topic of this thesis

The main purpose of this thesis is to calculate the stationary axisymmetric structure of a hydromagnetically driven relativistic jet. I will focus mainly on the collimating regime of the jet (from the region at the disk/black hole, where plasma gets lifted into a wind, up to the fully collimated asymptotic jet). The structure will be calculated by considering the force-free local force balance across the surfaces of constant magnetic flux. The two approaches previously done by Fendt (1997; from now on F1997a), who solved the axisymmetric structure including a *Kerr metric* of the black hole, and that of Fendt & Memola (2001; from now on FM2001) who calculated the axisymmetric structure in the special relativistic regime, but including *differential rotation* term of the magnetic field lines, will be combined in this approach. The differential rotation is needed because as the magnetic field emanates from the accretion disk it is likely to be rotating differentially. For a spinning black hole, its influence on the character of the electromagnetic fields has to be taken into account. This combination also allows for a consistent scaling of the jet-structure with the mass of the black hole. This will be done according to the top-down approach adopted by FM2001 for their calculations. The method to solve the force balance is based on a finite element solver, which has been developed for this purpose by Camenzind (1987), Haehnelt (1990), Fendt (1994, 1995, 1997) and Memola (2001).

The structure of this thesis is as follows: In Section 2 the assumptions

about the physics of the gas will be given. Also the Grad-Shafranov Equation (GSE), which describes the local force-balance across the surfaces of constant magnetic flux, will be derived. The method used to solve the GSE, including the necessary boundary conditions and the setup of the model, will be described in Section 3. In Section 4 the code developed for solving the finite element method will be explained and will be tested, by comparing the results with the results previously obtained by F1997a and FM2001. Finally the method developed in this thesis be discussed in Section 5. Also a set of possible interesting follow-up studies will be discussed. These include: 1) An alternative bottom-up approach to solve the GSE. 2) Calculating the Wind-Equation, the force-balance along the calculated magnetic flux-surfaces, and thereby obtaining parameters such as final velocities of the flow, enabling comparison of the model predictions to observed velocities. 3) Using the calculated magnetic flux-surface structure to calculate the polarization of synchrotron emission, that also might make comparison of the model with observations possible. Finally I will give a conclusion in Section 6.

Chapter 2

Magnetohydrodynamic Jets

2.1 Model assumptions

To describe the force-balance in the jet, the following assumptions have been made:

Black hole -Kerr metric- Because the jet originates close to the central black hole, it seems appropriate to include a general relativistic description of the space-time. The influence of the black hole on the space-time changes the behavior of the electromagnetic fields. A 3+1 split of the space-time (Thorne & McDonald 1984) around the black hole, with a mass M and a angular momentum per unit mass $a = \frac{J}{Mc}$, was adopted which is described by the following line-element in Boyer-Lindquist coordinates (Boyer & Lindquist 1967)

$$ds^2 = \alpha^2 c^2 dt^2 - \tilde{\omega}^2 \left(d\phi - \omega dt\right)^2 - \left(\rho^2/\Delta\right) dr^2 - \rho^2 d\theta^2 \tag{2.1}$$

Here t denotes a global time, in which the system is stationary, ϕ is the angle around the axis of symmetry (the polar axis). And r, θ are similar to the Euclidean spherical coordinates. The parameters of the metric are given by

$$\begin{array}{ll} \rho^2 \equiv r^2 + a^2 \cos^2\theta & \Delta \equiv r^2 - 2GMr/c^2 + a^2 \\ \Sigma^2 \equiv \left(r^2 + a^2\right)^2 - a^2 \Delta \sin^2\theta & \tilde{\omega} \equiv \left(\Sigma/\rho\right) \sin\theta \\ \omega \equiv 2aGMr/c\Sigma^2 & \alpha \equiv \rho\sqrt{\Delta}/\Sigma \end{array}$$

Where ω is the angular velocity of the differentially rotating space, or the angular velocity of an observer moving with zero angular momentum at infinity distance from the black hole (ZAMO), $\alpha = (d\tau/dt)$ is the redshift function, describing the lapse between the proper time τ in the ZAMO system to the global time t. The $\tilde{\omega}$ corresponds to the R component in a cylindrical coordinate system (R, Z) for $r \to \infty$. This split allows for a description of the magnetic and electric fields in a similar way to that in a flat Minkowski space-time. The angular velocity of the black hole is given by $\Omega_{\rm BH} = c^3 \left(a/2GM\right) \left(GM/c^2 + \left[\left(GM/c^2\right)^2 - a^2\right]^{1/2}\right)^{-1}$. We adopt throughout this thesis for the angular momentum per unit mass $a = 0.8M$.

Ideal magnetohydrodynamics: Our model is based on the assumption of ideal magnetohydrodynamics (MHD). MHD describes the dynamics of a conducting fluid in the presence of magnetic fields. Instead of treating each individual particle, MHD treats the dynamics of the average over a whole ensemble of particles. This ensemble can be considered as being a neutrally charged fluid, if charge separation cancels out on scales larger than the typical Debye length scale.

Ideal MHD considers the plasma conductivity to be infinite and diffusive processes are neglected. A result of this assumption is that the flux field lines are 'frozen' into the plasma (the flux fields move with the plasma).

The dynamics of a plasma under these assumptions are given by Maxwell's Equations (Eq. 2.2-2.5)

$$\nabla \wedge (\alpha \mathbf{B}) = \frac{4\pi}{c} \alpha \mathbf{j} - (\mathbf{E} \cdot \nabla \omega)\, \tilde{\omega} e_{\hat{\phi}} + \frac{\partial \mathbf{E}}{\partial t} \tag{2.2}$$

$$\nabla \wedge (\alpha \mathbf{E}) = (\mathbf{B} \cdot \nabla \omega)\, \tilde{\omega} e_{\hat{\phi}} - \frac{\partial \mathbf{B}}{\partial t} \tag{2.3}$$

$$\nabla \cdot \mathbf{B} = 0 \tag{2.4}$$

$$\nabla \cdot \mathbf{E} = 4\pi \rho_e \tag{2.5}$$

the equation of continuity

$$\left(N^{\alpha}\right)_{;\alpha} = \left(n u^{\alpha}\right)_{;\alpha} = 0 \tag{2.6}$$

and the equation of motion

$$T^{\alpha\beta}{}_{;\beta} = \left(T^{\alpha\beta}_{M} + T^{\alpha\beta}_{em}\right)_{;\beta} = 0. \tag{2.7}$$

Stationarity and axisymmetry The problem is simplified by assuming axisymmetry and stationarity. Because observations show that jets are generally collimated almost into a cylindrical shape and the time scales for typical rotations of the magnetic field lines in the disk are $> 10^4$ than the time scales for the jet-propagation, the assumption of axisymmetry is reasonable. The dynamic time scales for the collimation of the jet are much shorter than that of the dynamic time-scales of the propagation of the jet, and therefore stationarity seems a reasonable assumption as well. The advantage of these assumptions is that the problem, as we will show, is now constrained to a 2-D problem and has become much easier to solve.

It must be noted that although observations of jet-knots show asymmetries and time-variability which would seem to contradict our assumptions, we are primarily interested in the collimation and the global structure of the jet-flow, and therefore think the assumptions of axisymmetry and stationarity are valid in this case. However, ultimately the assumption of stationarity would have to be modified.

With the assumption of axisymmetry, a magnetic flux-function can be defined

$$\Psi\left(r,\theta\right) = \frac{1}{2\pi}\int \mathbf{B}_P \cdot d\mathbf{A} \tag{2.8}$$

$$\mathbf{B_P} = \frac{1}{\tilde{\omega}}\Psi \wedge \mathbf{m} \tag{2.9}$$

where the flux is taken through a loop of the Killing vector $\mathbf{m} = \tilde{\omega}^2\nabla\phi$. In the same way the poloidal current is defined by the current density measured through the same loop

$$I = -\int \alpha \mathbf{j}_P \cdot d\mathbf{A} = -\frac{c}{2}\alpha\tilde{\omega}B_T \tag{2.10}$$

The assumptions of axisymmetry and stationarity lead to conserved physical quantities as well:

First, stationarity implies a conservation of the mass flow rate $\dot{N}$ along the flux surfaces

$$\eta(\Psi) = \frac{d\dot{N}}{d\Psi} \tag{2.11}$$

Secondly, axisymmetry gives a conservation of the angular velocity of the field line (Ferraro's iso-rotation parameter Ω_F (Ferraro 1937)) that can be derived from the derivative of the time-component of the vector potential, $\Omega_F(\Psi) = -c\,(dA_0/d\Psi)$. In the special relativistic case, this can be thought off as the velocity of the gas minus the slide along the field lines

$$\Omega_F(\Psi) = -c\frac{1}{R}\left(v_\phi - \frac{\eta(\Psi)}{\rho}B_\phi\right) \tag{2.12}$$

The third conserved quantity is the total angular momentum per unit density

$$L(\Psi) = -\left(\mu + \frac{\overline{B}^2}{4\pi n}\right) l u_t - \frac{u_t\,(1-\Omega_F l)}{4\pi\eta}\overline{B}_\phi \tag{2.13}$$

Further the total energy is conserved

$$E(\Psi) = -\left(\mu + \frac{\overline{B}^2}{4\pi n}\right) u_t - \frac{u_t\,(1-\Omega_F l)}{4\pi\eta}\overline{B}_t \tag{2.14}$$

with $\mathbf{u} = (u_t, u_r, u_\theta, u_\phi)$ the four velocity vector.

Force-free approximation For the high velocities observed in highly relativistic jets, a high magnetization ($\sigma >> 1$) of the jet is needed (see for example Fendt et al. 1996). Here σ quantifies the magnetic flux in terms of mass flux (Michel 1969)

$$\sigma(\Psi) = \frac{\Psi_{\max} c}{4\pi\mu\eta(\Psi) R_L^2} \tag{2.15}$$

For a force-free jet the current density $I(\Psi)$ becomes a conserved quantity. In the case of high magnetization the inertial terms will be weak compared to the magnetic terms. We assume that the inertial terms can be neglected with respect to the magnetic forces when calculating the cross-field force balance in the collimating regime. This limit is called the force-free limit. The equation of motion reduces to

$$0 = \rho_e \mathbf{E} + \frac{1}{c}\mathbf{j} \wedge \mathbf{B} \tag{2.16}$$

To fully describe the magnetic jet formation this assumptions breaks down, because the collimated non force-free jet lies beyond the Alfvén and fast magnetosonic surfaces, where the plasma kinetic energy dominates the magnetic energy, which contradicts the assumption of force-freeness. Also the initial acceleration of the gas lifted from the accretion disk cannot be described by a force-free configuration.

Numerical calculations of the plasma motion along the field show that, for a high magnetization, the Alfvén Mach number remains relatively low. Thus the inertial curvature term should not play a dominant role. Contopoulos & Lovelace (1994) found from self-similar solutions that the centrifugal forces are dominated by magnetic forces.

It is therefore assumed that the calculated collimating jet structure with the assumption of force-free will not change dramatically if inertial terms were to be included.

2.2 Grad-Shafranov Equation (GSE)

The Grad-Shafranov Equation (GSE) describes the force-balance across the flux-fields[1]. In order to derive the GSE, the normal vector perpendicular to the flux-surface is introduced

$$\mathbf{n} = -\frac{\nabla\Psi}{|\nabla\Psi|} \tag{2.17}$$

the toroidal part of Ampère's equation (Eq. 2.2) can be rewritten as

$$\begin{aligned} 4\pi\alpha\mathbf{j_T} &= \nabla \wedge (\alpha \mathbf{B_P}) + (\mathbf{E}_P \cdot \nabla\Omega_F)\,\tilde{\omega} b f e_{\hat{\phi}} \\ &= \nabla \wedge \left(\frac{\alpha}{2\pi\tilde{\omega}^2}\nabla\Psi \wedge \tilde{\omega}\mathbf{e}_{\hat{\phi}}\right) - (\mathbf{E_P} \cdot \nabla\,(\Omega_F - \omega))\,\tilde{\omega}\mathbf{e}_{\hat{\phi}} + \\ &\quad (\mathbf{E_P} \cdot \nabla\Omega_F)\,\tilde{\omega}\mathbf{e}_{\hat{\phi}} \\ &= \nabla\Psi\left(\nabla \cdot \tilde{\omega}\mathbf{e}_{\hat{\phi}}\right)\frac{\alpha}{2\pi\tilde{\omega}^2} - \frac{\tilde{\omega}}{2\pi}\mathbf{e}_{\hat{\phi}}\nabla \cdot \left(\frac{\alpha}{\tilde{\omega}^2}\nabla\Psi\right) \end{aligned}$$

[1]This derivation follows that of Jensen (1997)

$$
\begin{aligned}
&+\frac{1}{2\pi}\left(\tilde{\omega}\mathbf{e}_{\hat{\phi}}\cdot\nabla\right)\left(\frac{\alpha}{\tilde{\omega}^2}\nabla\Psi\right)-\frac{\alpha}{2\pi\tilde{\omega}^2}\left(\nabla\Psi\cdot\nabla\right)\tilde{\omega}\mathbf{e}_{\hat{\phi}}\\
&+\frac{\Omega_F-\omega}{2\pi\alpha}\left(\nabla\Psi\cdot\nabla\left(\Omega_F-\omega\right)\right)\tilde{\omega}\mathbf{e}_{\hat{\phi}}-\frac{\Omega_F-\omega}{2\pi\alpha}\left(\nabla\Psi\cdot\nabla\Omega_F\right)\tilde{\omega}\mathbf{e}_{\hat{\phi}}\\
=&-\frac{\tilde{\omega}}{2\pi}\nabla\cdot\left(\frac{\alpha}{\tilde{\omega}^2}\nabla\Psi\right)\frac{\left(\Omega_F-\omega\right)}{\alpha}\cdot\\
&\left(\nabla\Psi\cdot\nabla\left(\Omega_F-\omega\right)-\frac{d\Omega_F}{d\Psi}|\nabla\Psi|^2\right)\mathbf{e}_{\hat{\phi}}\\
=&\,4\pi\alpha j^{\hat{\phi}}\mathbf{e}_{\hat{\phi}}
\end{aligned}
\tag{2.18}
$$

The only non-vanishing terms are

$$\rho_e\mathbf{E_P}+\mathbf{j_P}\wedge\mathbf{B_T}+\mathbf{j_T}\wedge\mathbf{B_P}=0$$

since $\mathbf{E_T}=0$, $\mathbf{j_P}\|\mathbf{B_P}$, and $\mathbf{j_T}\|\mathbf{B_T}$. The first component is taken from Gauss's law (Eq. 2.5)

$$4\pi\rho_e=\nabla\cdot\mathbf{E_P}=-\nabla\cdot\left(\frac{\Omega_F-\omega}{2\pi\alpha}\nabla\Psi\right)$$

$$\rho_e\mathbf{E_P}=\frac{1}{4\pi}\left[\nabla\cdot\left(\frac{\Omega_F-\omega}{2\pi\alpha}\nabla\Psi\right)\right]\frac{\Omega_F-\omega}{2\pi\alpha}\nabla\Psi \tag{2.19}$$

$$
\begin{aligned}
\mathbf{j_P}\wedge\mathbf{B_T} &= \left(\frac{\mathbf{e}_{\hat{\phi}}\wedge\nabla I}{2\pi\alpha\tilde{\omega}}\right)\wedge\left(-\frac{2I}{\alpha\tilde{\omega}}\mathbf{e}_{\hat{\phi}}\right)\\
&= \frac{1}{\pi\left(\alpha\tilde{\omega}\right)^2}\left[\left(-I\mathbf{e}_{\hat{\phi}}\cdot\mathbf{e}_{\hat{\phi}}\right)\nabla I-\left(-I\mathbf{e}_{\hat{\phi}}\cdot\nabla I\right)\mathbf{e}_{\hat{\phi}}\right]\\
&= -\frac{1}{\pi\left(\alpha\tilde{\omega}\right)^2}I\nabla I
\end{aligned}
\tag{2.20}
$$

$$\mathbf{j_T}\wedge\mathbf{B_P} = \left(j_{\hat{\phi}}\mathbf{e}_{\hat{\phi}}\right)\wedge\left(\frac{\nabla\Psi\wedge\mathbf{e}_{\hat{\phi}}}{2\pi\tilde{\omega}}\right)$$

$$
\begin{aligned}
&= \left(j_{\hat{\phi}}\mathbf{e}_{\hat{\phi}}\cdot\frac{\mathbf{e}_{\hat{\phi}}}{2\pi\tilde{\omega}}\right)\nabla\Psi-\left(j_{\hat{\phi}}\mathbf{e}_{\hat{\phi}}\cdot\nabla\Psi\right)\frac{\mathbf{e}_{\hat{\phi}}}{2\pi\tilde{\omega}}\\
&= \frac{1}{2\pi\tilde{\omega}}j_{\hat{\phi}}\nabla\Psi
\end{aligned}
\tag{2.21}
$$

$$
4\pi\alpha j_{\hat{\phi}}\nabla\Psi=-\frac{\alpha\tilde{\omega}}{2\pi}\left[\nabla\cdot\left(\frac{\Omega_F-\omega}{\alpha}\nabla\Psi\right)\right]\frac{\Omega_F-\omega}{\alpha}\nabla\Psi+\frac{8\pi}{\alpha\tilde{\omega}}I\nabla I \tag{2.22}
$$

$$
\begin{aligned}
4\pi\alpha j_{\hat{\phi}} &= -\frac{\alpha\tilde{\omega}}{2\pi}\left[\nabla\cdot\left(\frac{\Omega_F-\omega}{\alpha}\nabla\Psi\right)\right]\frac{\Omega_F-\omega}{\alpha}+\frac{8\pi}{\alpha\tilde{\omega}}I\frac{dI}{d\Psi}\\
&= -\frac{\tilde{\omega}}{2\pi}\nabla\cdot\left[\frac{\left(\Omega_F-\omega\right)^2}{\alpha}\nabla\Psi\right]+\frac{\tilde{\omega}}{2\pi}\frac{\left(\Omega_F-\omega\right)}{\alpha}\nabla\Psi\cdot\nabla\left(\Omega_F-\omega\right)\\
&\quad+\frac{8\pi}{\alpha\tilde{\omega}}I\frac{dI}{d\Psi}
\end{aligned}
\tag{2.23}
$$

$$
\nabla\cdot\left[\left(\frac{\alpha}{\tilde{\omega}}-\frac{\left(\Omega_F-\omega\right)^2}{\alpha}\right)\nabla\Psi\right]+\frac{\left(\Omega_F-\omega\right)}{\alpha}\frac{d\Omega_F}{d\Psi}|\nabla\Psi|^2+\frac{16\pi^2}{\alpha\tilde{\omega}}I\frac{dI}{d\Psi}=0 \tag{2.24}
$$

The Grad-Shafranov Equation with differential rotation of flux-fields then becomes

$$
\tilde{\omega}\nabla\cdot\left(\alpha\frac{D}{\tilde{\omega}^2}\nabla\Psi\right)=\tilde{\omega}\frac{\omega-\Omega_F}{\alpha c^2}\Omega_F^{'}|\nabla\Psi|^2-\frac{1}{\alpha\tilde{\omega}}\frac{4}{c^2}II^{'} \tag{2.25}
$$

with $D=1-\left(\tilde{\omega}/\tilde{\omega}_L\right)^2$ where $\tilde{\omega}_L^2=\left(\pm\alpha/\left(\Omega_F-\omega\right)\right.$, the positions of the two light surfaces. The gradients, expressed in terms of the Boyer-Lindquist coordinates are

$$
\nabla=\left(\frac{\Delta\left(r,t\right)}{\rho\left(r,t\right)}\frac{\partial}{\partial r},0,\frac{1}{\rho(r,t)}\frac{\partial}{\partial\theta}\right) \tag{2.26}
$$

We are left with Eq. 2.29, which is a parabolic 2-D non-linear partial differential equation, with two free function $\Omega_F\left(\Psi\right)$ and $I\left(\Psi\right)$ that have to be specified. Note that although the equation is two-dimensional, the force-balance described is a fully three-dimensional balance, which is reduced by

the assumption of axisymmetry (this is commonly called a 2.5-D solution instead of a 2-D or 3-D solution). This equation reduces for a constant Ω_F, and in the special relativistic regime, to the well-known Pulsar Equation (Michel 1973; Charleman & Wagoner 1973)

The GSE can be made more transparent by showing the different mechanisms contributing to collimation of the jet

$$\mathbf{n}\cdot(\mathbf{B_P}\cdot\nabla)\frac{\mathbf{B_P}}{4\pi}\left(1-M_A^2-x^2\Omega_F^2\right)=\left(1-x^2\Omega_F^2\right)\frac{\nabla_\perp B_P^2}{8\pi}+\frac{\nabla_\perp B_\phi^2}{8\pi}$$
$$+\nabla_\perp P+\left(\frac{B_\phi^2}{4\pi}-\rho u_\phi^2\right)\frac{\nabla_\perp x}{x}-\frac{B_P^2\Omega_F}{4\pi}\nabla_\perp\left(x^2\Omega_F\right) \tag{2.27}$$

The terms in the equation, which are indicated in red, are the inertial terms: the de-collimating centrifugal force due to the motion of the matter along the curved poloidal field line, the gas pressure gradient, the de-collimating due to the centrifugal force of the rotating plasma. For a force-free jet the balance is determined solely by the magnetic forces, so the curvature of the poloidal field lead to a tension force, also the poloidal magnetic field pressure reduced by the pressure gradient of the electric field. There are the toroidal magnetic pressure gradient and the collimating effect of the toroidal field tension. The last term combines the tension of the curved poloidal field and the effect of the space charge density.

If the force-free assumption is made the following balance between collimating forces (on the l. h. s.) and the de-collimating forces (on the r. h. s.) becomes

$$\mathbf{n}\cdot(\mathbf{B_P}\cdot\nabla)\frac{\mathbf{B_P}}{4\pi}+\frac{B_P^2\Omega_F}{4\pi}\nabla_\perp\left(x^2\Omega_F\right)+x^2\Omega_F^2\frac{\nabla_\perp B_P^2}{8\pi}=\frac{\nabla_\perp B_P^2}{8\pi}+\frac{\nabla_\perp B_\phi^2}{8\pi}+\frac{B_\phi^2}{4\pi}\frac{\nabla_\perp x}{x}$$

Light surfaces The light surfaces were already briefly mentioned before. For our stationary force-free approach, the GSE in Kerr metric has two singular surfaces, defined by $\tilde{\omega}_L^2=\left(\pm\frac{\alpha}{\Omega_F-\omega}\right)$, which are typical features for a relativistic treatment. The meaning of these surfaces can be understood by thinking of the magnetic fields flux-surfaces rotating at an angular velocity $\Omega_F(\Psi)$. These angular rotations can be expressed as a toroidal velocity like $v_\phi=\tilde{\omega}(r,\theta)\ \Omega_F(\Psi(r,\theta))$. When this toroidal velocity reaches the speed of light $v_\phi=\tilde{\omega}\ \Omega_F=c$, this gives the singular surface, hence the name. Note that the flux-fields represent no physical object, and therefore the velocity corresponding to Ω_F can exceed the speed of light. There is an inner surface, near the black hole, which is due to the frame-dragging effect of the metric, and outer surface far away from the black hole. In the asymptotic region

were the black hole's influence is negligible and flux surfaces are collimated into cylinders, the light surface is also called (asymptotic) light cylinder. As the electric field contributions scale with the asymptotic light cylinder $E_P = \left(\frac{R}{R_{\rm LC}}\right) B_P$, the light surface is also an indication where the relativistic effect become important.

2.2.1 Normalizing the GSE

The GSE is further normalized and made dimensionless

$$\begin{array}{ll} r \Leftrightarrow R_{\rm LC} r & \tilde{\omega} \Leftrightarrow R_{\rm LC}\tilde{\omega} \\ \omega \Leftrightarrow (1/R_{\rm LC})\,\omega & \Omega_F \Leftrightarrow (1/R_{\rm LC})\,\Omega_F \\ \nabla \Leftrightarrow (1/R_{\rm LC})\,\nabla & \Psi \Leftrightarrow \Psi_{\rm max}\Psi \\ I \Leftrightarrow I_{\rm max} I & \end{array}$$

Here $R_{\rm LC}$ denotes the asymptotic light cylinder. The coupling constant, with parameters typical for AGN's, in the source term now becomes

$$g_I = \frac{4 I_{\rm max}^2 R_{\rm LC}^2}{c \Psi_{\rm max}^2} = 4 \left(\frac{I_{\rm max}}{10^{12}\ {\rm A}}\right)^2 \left(\frac{R_{\rm LC}}{10^{16}\ {\rm cm}}\right)^2 \left(\frac{\Psi_{\rm max}}{10^{33}\ {\rm Gauss}}\right)^{-2}$$

The normalized GSE becomes the following equation

$$\tilde{\omega}\nabla\cdot\left(\alpha\frac{D}{\tilde{\omega}^2}\nabla\Psi\right) = \tilde{\omega}\frac{\omega-\Omega_F}{\alpha}\Omega_F^{'}|\nabla\Psi|^2 - \frac{g_I}{\alpha\tilde{\omega}} I I^{'} \qquad (2.29)$$

Note that only the second term in the source term has the coupling constant g_I (indicated in red) which depends on $I_{\rm max}$, $R_{\rm LC}$ and $\Psi_{\rm max}$, the term due to angular rotation of the flux surfaces has not.

It will show out later in this thesis, that especially the normalization of the Ω_F will pose a problem in the method we adopt to solve the GSE. The advantage of normalizing with respect to the asymptotic light cylinder is that the normalized GSE can be used to study more general solutions for jets, because these solutions are then in terms of the dimensionless asymptotic light cylinder, which can be scaled, in principle, to any physical scale. The main problem is, when trying to match this dimensionless solution to a physical scale, the physical scaling of the asymptotic light cylinder follows from the 2-D solution. But to solve the 2-D solution, it seems that the scaling is needed beforehand. This problem will be discussed in the next sections.

From now on we normalize $c = 1$, and $G = 1$. The gravitational radius then becomes $\mathrm{R_g} = \frac{MG}{c^2} = M$. By doing this, the spatial scales of the jet can be expressed directly into the mass of the central black hole.

Chapter 3

Solving the Grad Shafranov Equation

The GSE can be solved numerically by using a finite element code with the 'Galerkin Ansatz' (see Appendix A for full detail). This method can solve parabolic non-linear differential equations when a set of boundary conditions is given on a chosen grid. Therefore an appropriate set of 'physical' boundary conditions needs to be specified in order to solve the equation. Also the two free functions $\Omega_F(\Psi)$ and $I(\Psi)$ have to be specified. There are two approaches how to do this. The first, a top-down approach will be described in this section and used in the rest of this thesis. A second bottom-up approach will be discussed in §5.2.

3.1 Regularity condition at the light surface

At the light surface, the GSE becomes singular (at $D = 1 - \left(\frac{\tilde{\omega}}{\tilde{\omega}_L}\right)^2 = 0$). In principle singularities always pose a problem when solving the equations numerically. It would be useful to have the light surface at the boundary. In that case the boundary conditions along the light surface have to be specified. On closer inspection, the GSE shows to have an intrinsic boundary condition along the light surface. At the light surface the GSE reduces to

$$\frac{\alpha}{\tilde{\omega}}\nabla D\nabla\Psi = \tilde{\omega}\frac{\omega-\Omega_F}{\alpha}\Omega_F^{'}|\nabla\Psi|^2 - \frac{g_I}{\alpha\tilde{\omega}}II^{'} \tag{3.1}$$

With the normal on the boundary defined as $\mathbf{n} = -\frac{\nabla D}{|\nabla D|}$ this regularity

condition for Ψ is actually equivalent to an inhomogeneous Neumann-type boundary condition

$$\frac{\partial \Psi}{\partial n} = -\frac{\tilde{\omega}}{|\nabla D|}\frac{\omega - \Omega_F}{\alpha^2}\Omega_F^{'}|\nabla \Psi|^2 + \frac{1}{|\nabla D|}\frac{g_I}{\alpha^2}II^{'} \tag{3.2}$$

This offers the possibility to solve the structure of the flux-surfaces in two separate regions: 1) the inner region inside of the light surface and 2) the outer region outside of the light surface. Both of these regions havie the light surface as a boundary.

An estimate for whether the light surface lies within the jet so that this distinction can actually be used can be made by assuming a Keplerian rotation of the magnetic flux surfaces $\Omega_F(r) = \frac{1}{r^{3/2}+a} \propto r^{-3/2}$. For the light surface the relation $r_{\rm lc} = \Omega^{-1}(r_{\rm disk}) = r_{\rm disk}^{1.5}$ holds. For the light surface to be inside the jet, the light surface radius must be less than the jet boundary $x_{\rm jet} = f_{\rm exp} r_{\rm disk}$ (where $f_{\rm exp}$ is the expansion rate of the jet and $r_{\rm disk}$ the outer disk radius). Junor et al. (1999) measured for the M87 jet a lower limit for the expansion rate of $f_{\rm exp} \geq 3.3$ (fully collimated at 200 R_g and at the upper limit of the un-collimated region of 60 R_g). For the light surface to be inside of the jet this implies $r_{\rm disk}^{1.5} < f_{\rm exp} r_{\rm disk}$. This gives $r_{\rm disk} < f_{\rm exp}^2 \approx 10$ R_g which is a lower limit, because the actual formation region can be smaller than the resolved 60 R_g. Although the disk size we adopt is somewhat smaller, typical estimates for the expansion rate is about $f_{\rm exp} \approx 100$. In that case it is highly likely that the light surface will be inside the jet, and the distinction between an inner region and outer region can be made.

3.2 Boundary condition at the jet axis

We assume that there is no magnetic flux on the jet axis (R=0). On the jet axis a Dirichlet boundary condition is chosen of $\Psi = 0$.

3.3 Jet surface boundary condition

The outer surface of the jet is defined at $\Psi = 1$. For a flux distribution that is saturated at $\Psi = 1$, this is the last flux-surface that contains all of the poloidal magnetic field. For the jet surface, $\Psi = 1$ is chosen as the Dirichlet boundary condition. In the next section the determination of the shape of the boundary will be explained.

3.4 Disk and black hole boundary conditions

The magnetic field distribution along the disk is not well known. There have been some studies to calculate the disk structure around a black hole (e. g. Khanna & Camenzind 1992; Kudoh & Kaburaki 1996; Koide, Shibata & Kudoh 1998). Khanna & Camenzind (1992) obtained for a stationary axisymmetric thin disk a solution for the flux distribution along the disk: $\Psi \propto e^{-k^2 \int D(r')dr'}$ (See Fig. 3.1).

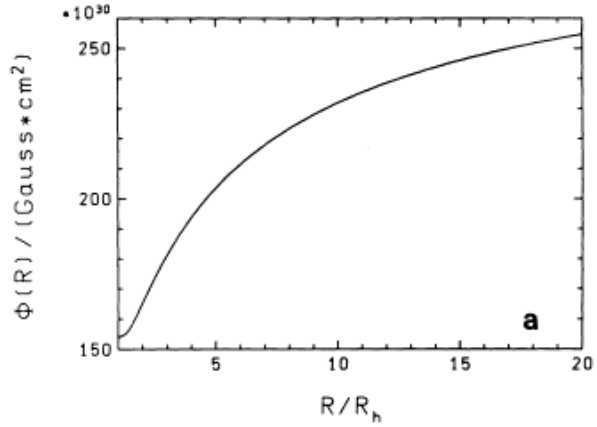

Figure 3.1: Calculated flux distribution at the surface of an axisymmetric thin magnetized accretion disk around a black hole (taken from Khanna & Camenzind 1992)

As mentioned before, it is possible for a black hole to have a magnetosphere (Blandford & Znajek 1974; Okamoto 1992; Kommissarov 2003). So it is possible for some magnetic flux to emerge from the black hole's direct environment. Because this process is yet poorly understood, we only assume that some fraction of the total flux Ψ_{BH} comes from the black hole's magnetosphere. As boundary condition we take for now a homogeneous Neumann boundary condition. There are some indications that the exact distribution close to the disk and central object do not have a large influence on the global solution, so for now these boundary conditions seem reasonable.

The boundary condition for the disk was chosen as

$$\Psi(x) = \Psi_{\rm BH} + \frac{(x - x_{\rm in}) / (A - x_{\rm in})^m}{1 + (x - x_{\rm in}) / (A - x_{\rm in})^m} \tag{3.3}$$

with

$$A = \frac{x_{\rm disk} - x_{\rm in}}{(\Psi_{\rm BH})^{-1/m}} + x_{\rm in} \tag{3.4}$$

This function is shown for different $\Psi_{\rm BH}$ in Fig. 3.2 in order to compare to the results of Khanna & Camenzind (1992).

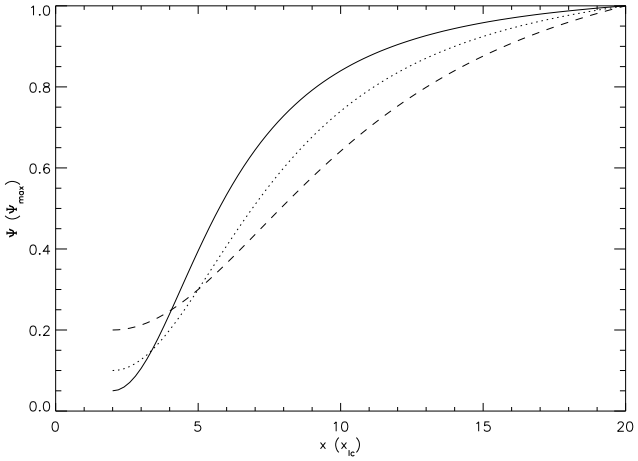

Figure 3.2: The boundary condition for different $\Psi_{\rm BH}$ with $m = 2$, for a disk with $x_{\rm in} = 2$ $R_{\rm g}$ and $x_{\rm disk} = 20$ $R_{\rm g}$.

3.5 Asymptotic solution for the special relativistic GSE

Appl & Camenzind (1991) showed that for a constant Ω_F, the boundary of the jet, defined at $\Psi = 1$, is known if some distribution $I(x)$ is assumed. With the Ansatz of $I(\Psi) = \left(1 - e^{-b\Psi}\right) / \left(1 - e^{-b}\right)$ the jet boundary is then given by $x_{\rm jet} = a\sqrt{e^b - 1}$. For a differentially rotating flux distribution, this position is not known in advance, so the GSE has to be solved somehow in

order to obtain this position. In order to obtain the boundary conditions along the collimated part of the flow the asymptotic version of the GSE is used.

The asymptotic behavior of a jet can be analyzed by considering the cross-field force balance of the relativistic GSE in the asymptotic region (region where $z >> R$)

$$R\nabla\cdot\left(\frac{1-\left(R\Omega_F\left(\Psi\right)/c\right)^2}{R^2}\nabla\Psi\right)=\frac{4}{c^2}\frac{1}{R}\frac{d}{d\Psi}I^2\left(\Psi\right)-R|\nabla\Psi|^2\frac{1}{2}\frac{d}{d\Psi}\Omega_F^2\left(\Psi\right) \quad (3.5)$$

By assuming perfectly collimated cylindrical or conical flows, the curvature of the poloidal field lines vanishes, and consequently the pressure gradients must be balanced by the radial directed forces and the toroidal pinch force (Heyvaerts & Norman 1989; Chiueh et al. 1991). An analysis of the asymptotic behavior of the Grad-Shafranov equation has been done for constant rotation (Appl & Camenzind 1991,1993) and for differential rotation of the flux fields F1997b. For high collimation ($\partial_x >> \partial_z$), the 2-D GSE, can be reduced to a one-dimensional equation. Because $\Psi\left(x,z\right)\rightarrow\Psi\left(x\right)$, the conserved quantities $\Omega\left(\Psi\right)$ and $I\left(\Psi\right)$ can be expressed as functions of x. If it is further assumed that the flux distribution is monotonous, the derivatives with respect to Ψ become $\partial/\partial\Psi\rightarrow\left(d\Psi/dx\right)^{-1}\left(d/dx\right)$. With these assumptions, Eq. 3.5 reduces to a ordinary differential equation in the first order in the derivative $\left(d\Psi/dx\right)^2$

$$\left(1-x^2\Omega_F^2\right)\frac{d}{dx}\left(\frac{d\Psi}{dx}\right)^2+\left(\frac{4}{x}-2x\Omega_F^2-x^2\frac{d\Omega_F^2}{dx}\right)\left(\frac{d\Psi}{dx}\right)^2+g\frac{dI^2}{dx}=0 \quad (3.6)$$

Because $\left(x^{-2}d\Psi/dx\right)^2$ is related to the magnetic pressure of the poloidal field ($\partial\Psi/\partial x=xB_z$), this equation can be rewritten as

$$\left(1-x^2\Omega_F^2\right)\frac{dy}{dx}-4xy\left(\Omega_F^2+\frac{x}{4}\frac{d\Omega_F^2}{dx}\right)=-\frac{g}{8\pi x^2}\frac{dI^2}{dx} \quad (3.7)$$

This has the formal solution

$$y\left(x\right)=\frac{1}{8\pi}\frac{1}{M\left(x\right)}\int_x^1\frac{1}{w^2}\frac{1}{1-w^2\Omega_F^2\left(w\right)}\frac{d}{dw}I^2\left(w\right)\cdot M\left(w\right)dw \quad (3.8)$$

with

$$M(x) = \exp\left[\int_1^x - \left(\frac{4w}{1 - w^2\Omega_F^2(w)} \cdot f(w)\right) dw\right] \tag{3.9}$$

and

$$f(x) = \Omega_F^2(x) + \frac{1}{4} x \frac{d}{dx}\Omega_F^2(x) \tag{3.10}$$

Because

$$\frac{d\Psi(x)}{dx} = x\sqrt{8\pi y(x)} \tag{3.11}$$

The asymptotic flux-distribution can be calculated by integrating $y(x)$

$$\Psi(x) = \int_0^x v\sqrt{8\pi y(v)}dv \tag{3.12}$$

The jet boundary x_{jet} is defined at the last flux surface $\Psi(x_{\text{jet}}) = 1$ and is therefore known. This will be used in order to solve the 2-D GSE.

3.5.1 Free functions $\Omega_F(x)$ and $I(x)$ of the GSE

As already mentioned, the functions $\Omega_F(\Psi)$ and $I(\Psi)$ have to be chosen when solving the GSE. As shown in the previous section, when trying to find a solution by integrating the asymptotic GSE one has to prescribe $\Omega_F(x)$ and $I(x)$ instead of $\Omega_F(\Psi)$ and $I(\Psi)$. This type of asymptotic solution has been studied before by Camenzind (1986), Appl & Camenzind (1993) and F1997b.

They adopted a bounded current distribution (often used in fusion research)

$$I(x) = B\frac{(x/a)^n}{1 + (x/a)^n} \tag{3.13}$$

The parameter a represents the radial scale on which the current rises, also called the 'core radius' of the jet and $B = \frac{1}{1-e^{-b}}$ where b is the 'pinch' of the current with respect to the flux fields. For constant rotation, this leads to the analytical solution for the asymptotic flux distribution as Appl & Camenzind (1993) found

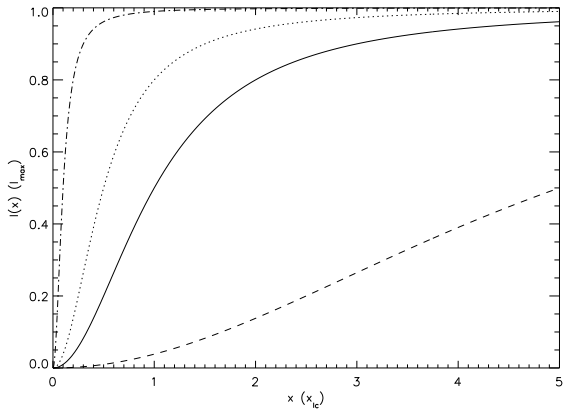

Figure 3.3: Current distribution $I(x) = B\frac{(x/a)^n}{1+(x/a)^n}$ for different core radii a. Shown are $a = 5.0$ (dashed), 1.0 (solid), 0.5 (dotted) and 0.1 (dash-dot), with $B = 1$.

$$\Psi(x) = \frac{1}{b}\log\left(1 + \left(\frac{x}{a}\right)^2\right) \tag{3.14}$$

We assume that the flux fields corotate with the accretion disk at Keplerian speed $\Omega_F(r) = \frac{1}{r^{3/2}+a}$ (the dimension of r is in R_g), the differential rotation profile $\Omega_F(x)$ in the asymptotic region will be a monotonous decreasing function of x as well, as flux distribution along the disk is assumed to be a monotonous increasing function. To investigate the influence of the differential rotation of the flux field, F1997b introduced a decreasing exponential rotation law for the asymptotic rotation profile

$$\Omega_F^2(x) = e^{h-hx} \tag{3.15}$$

where the parameter h is the steepness of the profile, and Ω_F is normalized to the asymptotic light cylinder $\Omega_F(1) = 1$.

If the asymptotic solution $\Psi(x)$ has then been found, it can then be applied to the 2-D GSE by creating the functions $\Omega_F(\Psi)$ and $I(\Psi)$ by combining $\Psi(x)$ with $\Omega_F(x)$ and $I(x)$. This is a top-down approach, i. e. the internal global solution of the jet is determined by the solution in the asymptotic regime. An alternative bottom-up approach is physically more plausible than the top-down approach. This is because the jet is created at the disk,

so it the properties like current- and rotation distribution will be tightly related to the disk physics. The bottom-up approach directly couples the jet structure to the physical processes at the disk surface. Unfortunately, the bottom-up approach is harder to solve than the top-down approach. In Section 5.2 the problems that arise when using this approach will be discussed and a method is proposed how to solve these problems. In Section 3.5.4 the disadvantages of using the asymptotically determined distributions for $I(\Psi)$ and $\Omega_F(\Psi)$ will be discussed.

3.5.2 The asymptotic light surface

It is interesting to note that apart from the singularity at x=1, the asymptotic GSE can contain a second singularity. This fact has not been mentioned before anywhere in the literature. If the differential rotation profile from Eq. 3.15 is taken, for the singular point, the following equation holds:

$$0 = 1 - x^2\Omega_F^2 = 1 - x^2 e^{h-hx} \tag{3.16}$$

This is by normalization automatically fulfilled at the asymptotic light cylinder $x = 1$, but also for $h = \frac{1}{1-x}\log\left(\frac{1}{x^2}\right)$. In Fig. 3.4 the toroidal velocity of the flux field is shown for $h = 0.2$, 0.5, 0.9, 1, 2 and 3.

It can be seen that for $h = 2$, the singularities merge at $x = 1$, because only one solution is possible. The first singularity is always thought to be the boundary between the sub-relativistic jet ($v_\phi < c$) and relativistic ($v_\phi > c$). The origin of this second singularity in the 1-D equation can be clarified if the 2-D equation is considered. As can be seen in the Fig. 3.5, the second singularity can be interpreted as the same light cylinder as at $x = 1$, after which the asymptotic relativistic regime of the jet becomes sub-relativistic again.

Note that this holds for any rotation profile which is monotonously decreasing, where $\Omega_F(1) = 1$ and for $x > 1$, $\Omega_F(x) \propto x^n$, with $n \geq 2$. This is a restriction to the configuration of the relativistic jet in this model. The flux field that passes through the light surface is not able to pass it for a second time, but has to collimate before the second light surface. Otherwise, this would imply a contradiction. Because for the first light cylinder $x\Omega_F(\Psi) = 1$. As the flux field crosses the first light cylinder, x will only increase. It is therefore not possible to get $x\Omega_F(\Psi) < 1$ after the crossing. So it should be possible to have a core structure in the jet, where a relativistic

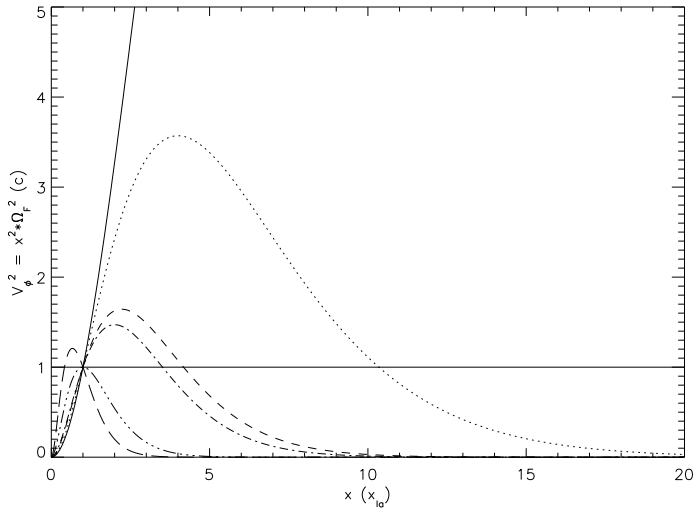

Figure 3.4: Toroidal velocity $v_\phi = x^2\Omega_F^2$ for different steepness ($h = 0.2$ (solid), 0.5 (dotted), 0.9 (dashed), 1.0 (dash dot) and 2.0 (dash 3xdot) 3.0 (long dashes)). The line indicates the position of the regular points at $x\Omega_F = 1$.

core is nested inside a sub-relativistic structure. Although it has not been mentioned in the literature on stationary work, it is interesting to note that similar configurations have been seen in the time dependent simulations of Casse & Keppens (2002) in a non-relativistic treatment including the disk. There the Alfvénic surface returns into the asymptotic region. As for high magnetizations the Alfén surface approaches the light surface, this would imply the same type of configuration. It is not clear however, how general this type of configuration is.

The model used in this paper is for now unable to handle such a configuration, because the distinction between an inner part (inside of the light surface) and an outer part cannot be made anymore and the position of the light surface becomes a much more complicated problem. We therefore focus on configurations that do not have a returning light cylinder. We will discuss the consequences of this assumption in § 5.1.

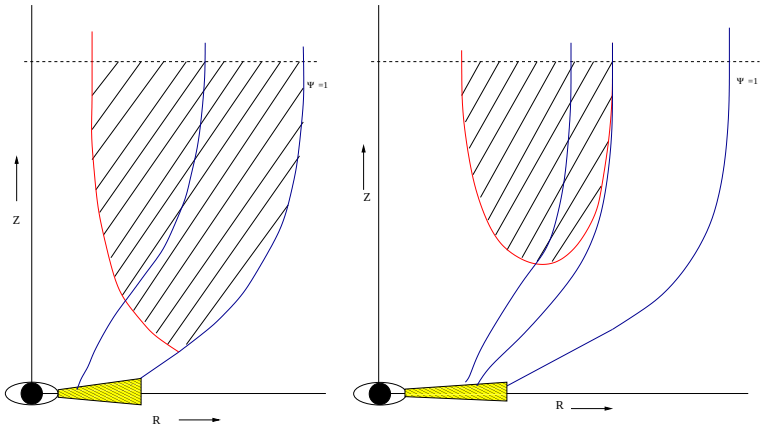

Figure 3.5: Two possible configurations for light surface. On the left: The boundary of the jet crosses the light surface. On the right: The light surface 'returns' to the asymptotic region. In this case a relativistic core is embedded in a subrelativistic envelope. The hatched regions indicate the regions where $x\ \Omega_F \geq 1$.

3.5.3 Solving the asymptotic GSE

To solve the asymptotic GSE, a program was written using IDL. The numerical integration was done using a Romberg solver, of 5th order (e. g. Stoer & Bulirsch 1980). The two singularities posed a small problem, because the function $M(x)$ is not defined at these points. This was solved by integrating either until 0.99999 or from 1.0001. Because the function within the integration blows up to $-\infty$, due to the exponential, this dies off, so as x approaches 1, the integral of the part between 0.99999 and 1.0001 will not contribute much to the total. To test how accurate the integration routine was, the results were compared to the analytical solution $\Psi(x) = 1/b \log\left(1 + \left(\frac{x}{a}\right)^2\right)$ by Appl & Camenzind (1993) for constant rotation and to the numerical results for the steepness parameter $h = 0.2$, and with $a = 1$ and $B = 1$ by Fendt (1997). The solutions and the relative differences are plotted with their analytical and numerical counterparts in Fig. 3.6 and Fig. 3.7. The results were accurate enough. The difference between the analytical solution of the asymptotic GSE and the numerical solutions were about 0.3% which seems to be a systematic error of 0.3% probably due to the integration limits of 0.99999 and 1.0001. Our solutions differed from that of Fendt (1997) within less than 0.05%. It is not surprising that no systematic error is seen

in Fig. 3.7, because the integrating limits are the same as Fendt (1997) used, so almost the same systematic error will be expected.

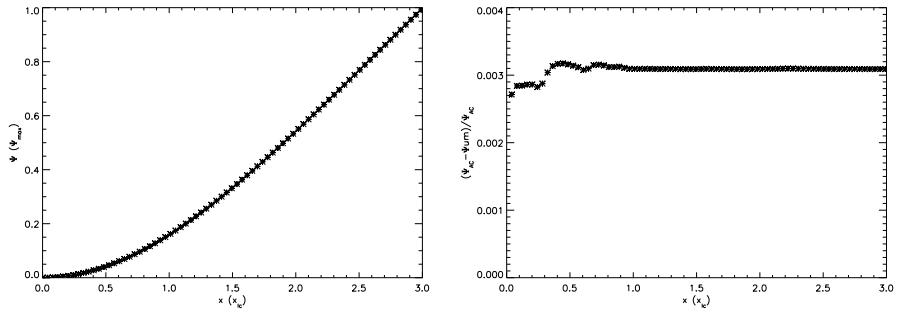

Figure 3.6: On the left: The values for $\Psi_{\rm num}\,(x)$ (solid line) using the IDL routine and over-plotted the analytical solution of Appl & Camenzind (1991) (crosses). On the right: The relative difference of the $(\Psi_{\rm AC} - \Psi_{\rm num})\,/\Psi_{\rm AC}$. A systematic error can be seen of about 0.3% with a scatter on much smaller scales.

3.5.4 Scaling the 2-D solution to the central mass of the black hole

FM2001 solved the special relativistic axisymmetric Grad-Shafranov Equation (GSE) including the differential rotation effect in the source term of the GSE. Their whole axisymmetric structure was normalized in terms of the asymptotic light cylinder radius $x_{\rm lc}$. An Ansatz was made for the rotation profile (see Eq. 3.15) and then the axisymmetric solution could be obtained. Their finding was, that their adopted steepness of the rotation profile was too low to match the Keplerian rotation at the foot-points of the field lines in the disk.

In order to use the solutions of the special relativistic asymptotic GSE, as a boundary condition for the general relativistic axisymmetric GSE, this solution had to be re-normalized, because the spatial coordinates in the general relativistic code were normalized to gravitational radii ($\rm R_g$) instead of the asymptotic light cylinder ($x_{\rm lc}$) as was the case with FM2001. Because the different normalization might cause confusion, the asymptotic solution will be expressed in terms of x, which is normalized to the asymptotic light

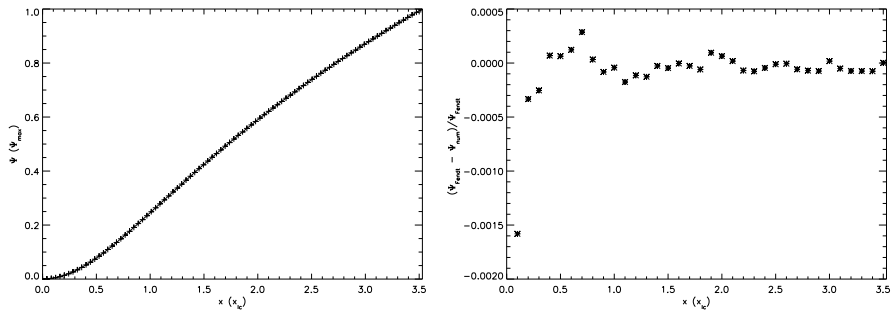

Figure 3.7: On the left: The values for $\Psi_{\mathrm{num}}(x)$ (solid line) using the IDL routine and over-plotted the numerical solution $\Psi_{\mathrm{Fendt}}(x)$ (crosses) used by Fendt (1997) (obtained using MATLAB). On the right: The relative difference $(\Psi_{\mathrm{Fendt}} - \Psi_{\mathrm{num}})/\Psi_{\mathrm{Fendt}}$.

cylinder x_{lc}, and the general relativistic GSE is expressed in terms of r which is normalized in gravitational radii $\mathrm{R_g}$.

Because the angular velocity of the flux fields $\Omega_F(\Psi)$ is conserved along Ψ, the rotation originating from the foot-point of the flux fields at the disk, which rotates at Keplerian speed, must have the same value in the asymptotic part. The Keplerian angular velocity distribution near a black hole is given by

$$\Omega_F(r) = \frac{1}{r^{3/2} + a} \tag{3.17}$$

with a the angular momentum per mass of the black hole. This reduces to the Newtonian Kepler profile for small a/r. The adopted profile for the asymptotic collimated jet is given by

$$\Omega_F(x) = \sqrt{e^{h-hx}} \tag{3.18}$$

Because $\Psi = \Psi(x)$ is known and $\Omega_F(x)$ in the asymptotic region, also $\Psi(\Omega_F)$ is known. This is also true for the foot-points $\Psi = \Psi(r)$ and $\Omega_F(r)$ are known and therefore $\Omega_F(\Psi)|_{\mathrm{asy}}$ can be related to $\Omega_F(\Psi)|_{\mathrm{Kerr}}$. By normalizing the asymptotic light surface, the asymptotic rotation profile can be used in the GSE normalized in $\mathrm{R_g}$ (see Fig. 3.8).

The question is now how from the chosen asymptotic distributions of $\Omega_F(x)$, $I(x)$ and $\Psi(x)$ a distribution is obtained that resembles the actual

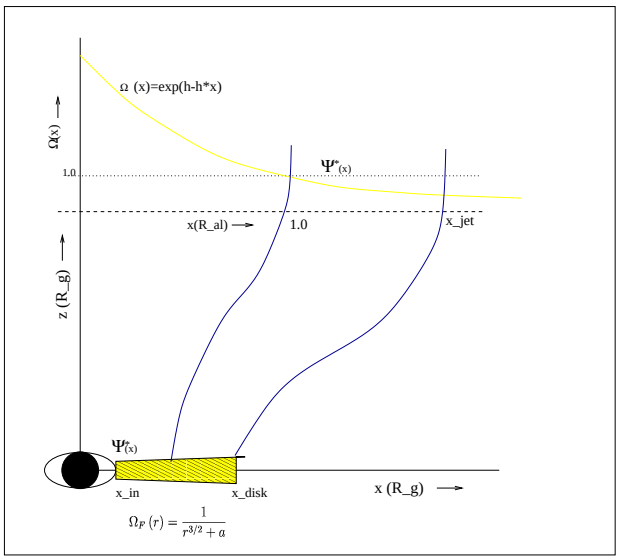

Figure 3.8: Connection the rotation distributions in the two regimes with different normalization of the rotation profile. At the top an exponential profile normalized to 1 at the light cylinder. At the bottom a Keplerian rotation law for the disk.

disk physics as closely as possible. So what kind of steepness h and what value for the asymptotic light cylinder in term of gravitational radii had to be adopted to fit the asymptotic exponential profile to the Keplerian profile at the disk. The disk size restricts the combination of jet radius and steepness somewhat. Given a disk size, the fraction between the maximal and minimal angular velocities for respectively the inner disk radius, and the outer disk disk radius

$$f_\Omega|_{\rm kep} = \frac{\Omega_{\rm max}}{\Omega_{\rm min}}|_{\rm kep} = \frac{r_{\rm disk}^{3/2}+a}{r_{\rm in}^{3/2}+a} \tag{3.19}$$

where for $r_{\rm in} \approx 2.0$ the radius of the ergosphere of the BH has been taken, and $r_{\rm disk}$ is the outer disk radius where the last flux emerges. In order for the asymptotic rotation profile to fit a Keplerian profile the fraction of maximal

and minimal angular velocities in the asymptotic region must be greater or equal to that of the flux from the disk. If it is equal, all the flux solely originates from the accretion disk. If it is larger, part of the flux comes from the ergosphere of the black hole.

$$f_\Omega|_{\rm asy} = \frac{\Omega_{\rm max}}{\Omega_{\rm min}}|_{\rm asy} \geq \frac{\Omega_{\rm max}}{\Omega_{\rm min}}|_{\rm kep} \tag{3.20}$$

or

$$f_\Omega|_{\rm asy} = \sqrt{\frac{e^h}{e^{h-hx_{\rm jet}}}} = \sqrt{e^{hx_{\rm jet}}} \geq \frac{r_{\rm out}^{3/2}+a}{r_{\rm in}^{3/2}+a} \tag{3.21}$$

FM2001 found a solution for a jet with $h = 0.9$, $x_{\rm jet} = 2.2\ x_{\rm lc}$, $x_{\rm in} = 0.05\ x_{\rm lc}$ and $x_{\rm disk} = x_{\rm disk} = 0.2\ x_{\rm lc}$. Relation 3.20 then becomes

$$f_\Omega|_{\rm asy} = \sqrt{e^{0.9\cdot 2.2}} = 2.69 > \frac{0.2^{3/2}}{0.05^{3/2}} = 8.0 \tag{3.22}$$

In Fig. 3.9 this situation is illustrated. This easily shows, as they already concluded, that the rotation profile they assumed was too flat to fit a Keplerian rotation profile at the disk. In order to get a disk with a Keplerian profile one would therefore need either a steeper profile (higher h) or a wider jet in terms of asymptotic light radii (lower g_I). This will part of the discussion in § 5.1. The disk physics are yet still not fully understood as well. For pressure supported disks, the rotation will be in general sub-Keplerian. As we take the disk as a boundary, it is difficult to say anything about the disk based on our solutions. A broader parameter study of our model as well as the bottom-up approach (See Section 5.1) is needed in order to address this problem.

One can ask whether it is possible to have any light cylinder radius for the asymptotic solution, when it is applied as a boundary condition to the 2-D problem. Because this radius determines how the $\Omega_F|_{\rm asy}$ is to be normalized ($r_{\rm lc}\ \Omega_F\left(r = r_{\rm lc}\right)|_{\rm disk} = 1$, but $\Omega_F\left(x = 1\right)|_{\rm asy} = 1$) . Depending on the distribution $\Psi\left(r\right)|_{\rm disk}$ along the disk, there is some $\Psi^*\left(r\right)|_{\rm disk}$, that collimates in the asymptotic regime at the light cylinder. This then gives some $\Omega_F\left(r\right)|_{\rm disk}$ that in its turn determines the asymptotic light cylinder radius. But which

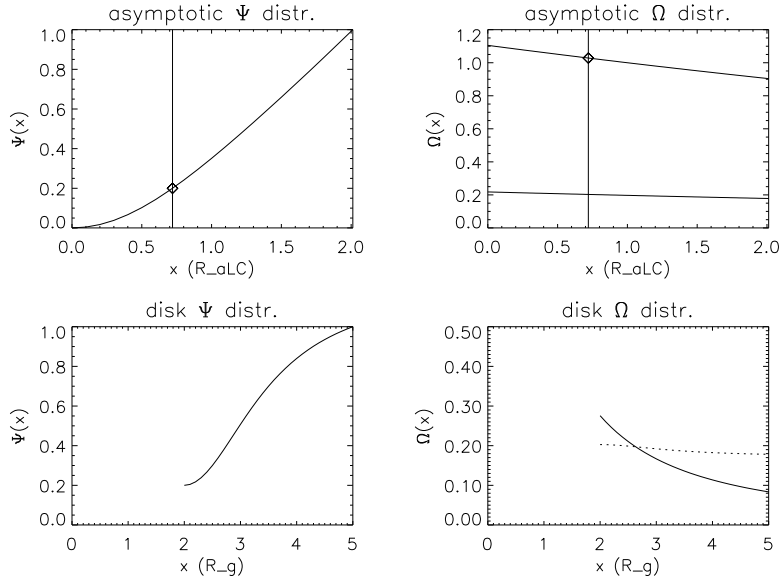

Figure 3.9: Comparison of asymptotic $\Omega_F = \sqrt{e^{h-hx}}$, with $h = 0.2$, $g_I = 2.71$, $x_{\rm disk} = 5.0$ $R_{\rm g}$ and $\Psi_{\rm BH} = 0.2$ and a Keplerian rotation profile at the disk. The solution of the asymptotic GSE (left top) gives some value for $\Psi(x)$, this corresponds to a Ψ along the disk (left bottom), that in turn gives the physical scaling of the asymptotic rotation profile (right top) using a Keplerian rotation profile at the disk (right bottom, solid line). In the right bottom figure, the normalized asymptotic solution (striped line) is shown to have an idea what this physical rotation law this normalization implies for the disk.

$\Psi^*(r)$ actually collimates is determined again by the 2-D solution, so this poses a problem.

Let us consider the Alfvén point that is determined by the conserved quantities as follows:

$$M_A^2 = 1 - \Omega_F(\Psi) L(\Psi) / E(\Psi) \tag{3.23}$$

In the force-free case ($M_A^2 << 1$), the Alfvén point approaches the light cylinder, so then

$$\Omega_F(\Psi) = E(\Psi) / L(\Psi) \tag{3.24}$$

As we know, the light cylinder is defined as $x_{\rm lc}\Omega_F(\Psi(x_{\rm lc})) = 1$ so the

light cylinder radius is determined by

$$x_{\mathrm{lc}} = L\left(\Psi\right)/E\left(\Psi\right) \tag{3.25}$$

So when the distribution along the disk is known and with it the $L\left(\Psi\right)$ and $E\left(\Psi\right)$, then the asymptotic light cylinder still is not defined uniquely beforehand. Because this relation might hold for any Ψ^* along the disk and beforehand it is not known which Ψ^* collimates exactly at the asymptotic light cylinder. This is determined by the 2-D solution.

In the top-down approach the value for the asymptotic light cylinder radius x_{lc} can be chosen arbitrarily in principle (as long as $\Omega_F\left(r\right)|_{\max} < \Omega_{\mathrm{BH}}$), but this choice then determines the conditions $L\left(\Psi\right)$ and $E\left(\Psi\right)$ at the disk. If for example the physics of the disk are known, then to get the 2-D structure of the jet, the asymptotic light cylinder has to be chosen in such a way that these match, and is therefore not free of choice. This apparent free choice of the asymptotic light cylinder radius is a consequence of the top-down approach. With the alternative bottom-up approach one does not have this problem, as will be explained in § 5.2.

3.6 Grid boundaries

3.6.1 Light surface

One of the main problems in solving the GSE was to find the correct grid. Because the light surface is the singular surface of the GSE (see §4.1), it is important that our boundaries for the inner grid as well as the outer grid follow the light surface as accurately as possible. The inner and outer light surfaces are given by

$$\tilde{\omega}_L^2 = \left(\pm\frac{\alpha}{\Omega_F - \omega}\right)^2 \tag{3.26}$$

To see what the light surfaces for a given Ω_F look like, this equation can be rewritten. At the light surface $\tilde{\omega} = \tilde{\omega}_L$ then

$$\Omega_F\left(r,\theta\right) = \pm\frac{\alpha\left(r,\theta\right)}{\tilde{\omega}\left(r,\theta\right)} + \omega\left(r,\theta\right) \tag{3.27}$$

On the right hand side of the equation there are only parameters of the Kerr metric. It is possible to calculate the family of solutions that satisfy Eq. 3.27 for all (r, θ). Every constant Ω_F then constitutes a contour on this surface that $\Omega_F(r, \theta)$ builds. In Fig. 3.10 the contours are shown for different constant Ω_F. It can be seen that for the outer light surface, the light surface moves outwards for smaller Ω_F (a higher radius is needed in order to maintain $x\ \Omega_F(\Psi(x)) = 1$). For the inner light cylinder, which is due to the frame dragging effect of the rotating black hole, the light surface moves inwards for higher Ω_F and approaches the black hole surface.

For a constant rotation of the flux fields the light surface can be calculated explicitly. This is different for a differentially rotating flux distribution. It is only known for a flux field Ψ with an $\Omega(\Psi)$ that if it crosses the light surface it will cross the light surface somewhere along the known surface of constant Ω_F as plotted in Fig. 3.10. At which point along the light surface it will cross depends on the internal force balance.

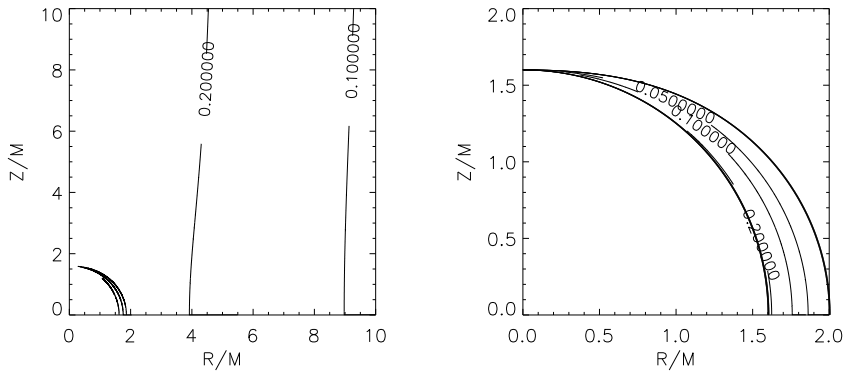

Figure 3.10: On the left, Inner- and outer light surfaces for different $\Omega_F = 0.05, 0.1, 0.2$. On the right: Inner light surfaces blown up. The black hole surface and the ergosphere are indicated as well (dashed).

The problem is that Ω_F is now a function of $\Psi(x)$, which is exactly what is to be calculated: The shape of our boundary is a result of our calculation for which this shape is needed. A procedure to solve this problem was proposed by FM2001: For the initial light surface boundary the light surface of the angular velocity of the asymptotic solution $\Omega_{F,\infty}$ is taken. For this grid the solution is calculated with the n-element solver algorithm, so $\Omega_F(\Psi)$ is known at the boundary. This boundary will differ from the real light surface by $D = 1 - \left(\frac{\tilde{\omega}}{\tilde{\omega_F}}\right)^2 = 1 - \left(\frac{\tilde{\omega}(\Omega_F(\Psi)-\omega)}{\alpha}\right)^2$. Then the grid is changed with $\Delta x \propto D(x,z)^2$. This procedure is repeated until $D(x,z) \approx 0$. FM2001 showed that this procedure successfully converges to the light surface as determined by a consistent axisymmetric solution.

3.6.2 Outer jet surface

The same problem as with the light surface holds for the outer boundary of the jet. The position of the boundary has to be specified in order to solve the internal solution, but this position itself depends on that solution. In principle the correct boundary can be searched for. To have an idea where to start, the asymptotic GSE is first solved. This gives the position $x_{\rm jet}$ of the last flux surface in the collimated asymptotic region. The correct shape of the boundary is the one that gives an consistent internal solution. Whether the internal solution is consistent is determined at the light surface. This 'matching problem' was studied by Fendt (1994). The internal solution is a consistent solution to the 2-D GSE, if at the light surface the transition of the flux surfaces across the light surface is smooth.

In order to find the correct solution the matching problem had to be solved, i. e. a correct boundary for $\Psi = 1$ had to be found consistent with the smooth crossing of the light surface. We chose to parameterize the outer boundary of the jet by some general function as F1997b and FM2001 did. For $Z > Z_{\rm yso}$ the grid was divided evenly in $dZ = (Z_{\rm max} - Z_{\rm yso})/n_{\rm el,Z}$ with $n_{{\rm el},Z}$ the number of elements in Z direction. Here $Z_{\rm yso}$ was chosen at double the height of the crossing of the jet boundary at opening angle θ_0 with the light surface $2Z_{\rm ls,min}$. We start at a fully collimated boundary down to $f_{\rm yso} \cdot Z_{\rm yso}$. For the rest of the i elements the function $R_i = R_{\rm jet} - dR\,(i - i_{\rm yso})^n$ was taken. The parameters $Z_{\rm yso}$, $f_{\rm yso}$, dR and n were a free choice, enabling a wide variety of shapes for the outer boundary (see Fig. 3.12).

The solution of the GSE searched for is the combination of coupling con-

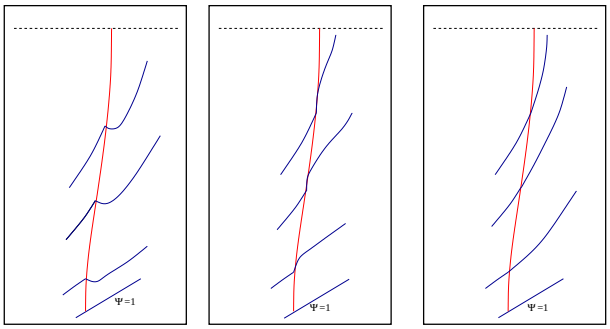

Figure 3.11: (Mis)match of the crossing flux surfaces at the light surface. The red line indicates the light surface. The blue lines indicate the magnetic flux surfaces. There are three possible configurations: The first two solutions do cross the light surface smoothly. Only the third solution has a smooth crossing of the light surface, and therefore the boundary corresponding to the internal force-balance.

stant g_I, core-radius a, and steepness h that gives a consistent match at the light surface for the inner and outer solution. Three possible situations at the light surface, that might occur while matching the inner solution to the outer solution, are shown in Fig. 3.11. Calculated examples of the matching problem will be shown in the next section. The first two configurations in Fig. 3.11 show a kink-like crossing at the light surface, which would require jumps in the magnetic field distribution which are not present in the asymptotic distribution. These are only due to the mismatch of the adopted outer boundary with the internal solution that is defined by the given combination of coupling constant g_I, core-radius a, and steepness h. The outer boundary is then adjusted to have about the same shape as the internal field lines close to the boundary. This adjustment is repeated until the match at the light surface is found.

3.6.3 Disk & black hole boundaries

At the lower part of the grid, the disk and black hole are taken as boundaries. The disk is assumed to be thin ($Z = 0$) and starts from the ergosphere ($r_{\rm in} = 2\ {\rm R_g}$), which is somewhat less than the marginally stable orbit (for a black hole with $a = 0.8$, $r_{\rm ms} \approx 3\ {\rm R_g}$) and the disk goes out to $r_{\rm disk}$.

In principle it would be logical to take the inner light surface inside of the

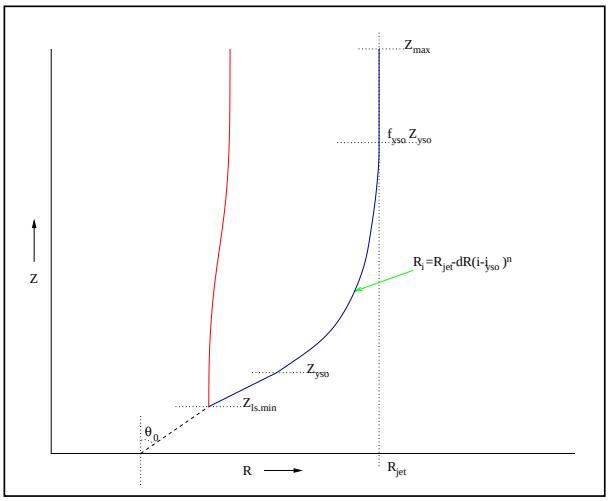

Figure 3.12: The parameterization of the outer boundary of the jet. The parameters $Z_{\rm yso}$, $f_{\rm yso}$, dR and n were a free choice.

ergosphere as a boundary near the black hole, because there then we have a well defined boundary condition. In order to use this boundary an iterated procedure to find this position is needed as well. The inner light surface could be found by starting at the light surface for the lowest rotation, which is furthest out from the horizon. Then the same iteration procedure as used for the outer light surface could be used to move the inner boundary to the inner light surface. This procedure will be very slow, because both the inner and outer iteration procedures have to occur at the same time, as they depend on each other. Because in general it is not clear how the flux emanates from the black hole's environment, we take for now the ergosphere as boundary.

3.6.4 Summary of the jet-model

The previous sections can be summarized as follows: The force balance across the magnetic flux surfaces, that emanate from an accretion disk and the central black hole's environment and collimates into a jet, is calculated in two regions: inside and outside of the light surface. The boundary conditions at the disk are based on both phenomenological arguments (for the black holes magnetosphere, based on Blandford & Znajek 1974; Okamoto 1992) and studies of magnetized accretion disks (e. g. Khanna & Camenzind 1992). It

is assumed that all of the magnetic flux collimates in the asymptotic region. The boundary condition in the asymptotic regime is provided by solving the 1-D asymptotic GSE of a collimated jet structure.

The grid for the inner region to be calculated is seen in Fig. 3.13. An opening angle θ_o is defined at the disk boundary $r_{\rm disk}$ from which the jet boundary extends to the light surface. The grid-boundaries are given by the jet-axis, black holes ergosphere, disk, jet boundary and the asymptotic jet.

The grid for the outer region to be calculated is seen in Fig. 3.14. An outer boundary is defined that starts at the crossing point from the internal region's boundary up to the jet radius $x_{\rm jet}$ in the asymptotic part.

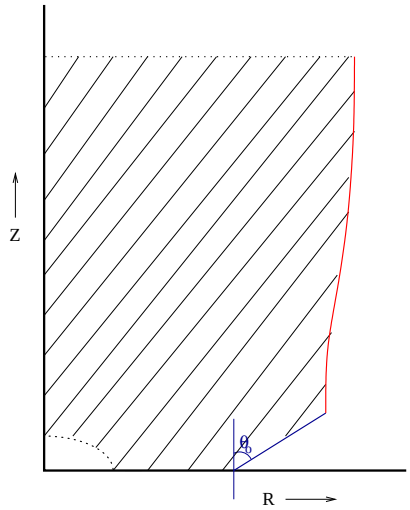

Figure 3.13: The inner region: Calculation for the region inside the light surface. The boundaries are given by the jet axis, the black hole ergosphere, the thin disk, the jet boundary given by an adopted opening angle θ_o of the last flux surface, the light surfaces and the asymptotic collimated region.

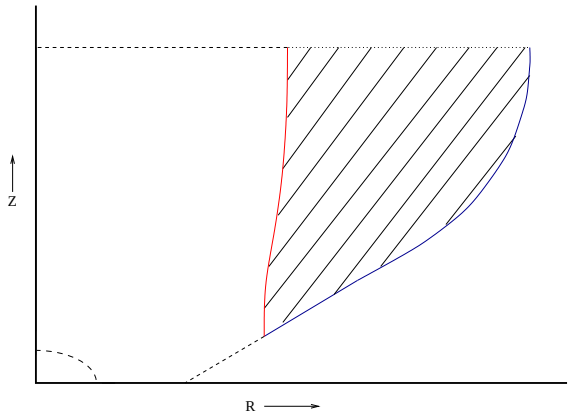

Figure 3.14: The outer region: Calculation for the region outside of the light surface. The boundaries are given by the light surface, the asymptotic solution that defines $x_{\rm jet}$ and the adopted outer jet boundary which is connected to the point at the light surface where internal flux crosses it at some opening angle θ_0.

Chapter 4

Code Development/Testing

4.1 Developing the code

The FORTRAN77 code for the finite element solver that included the Kerr metric in the GSE (see F1997a) was used as a base to develop the necessary code. The main idea behind the code was as follows: First a non-equidistant grid was specified. Then the Dirichlet conditions were specified for each (r, θ). An initial first guess for $\Psi(r, \theta)$, was given by applying the asymptotic solution to the whole grid. This proved to be a good choice for fast convergence of the code. The initial solution was then used to solve the equation 6.8. The maximal difference between the old and new value for Ψ was then used to estimate the degree of convergence. This procedure was repeated until the maximum difference $|\Psi_{\text{new}} - \Psi_{\text{old}}|_{\max} < \epsilon_{\text{conv}}$. We chose for the converging factor $\epsilon_{\text{conv}} = 1\ 10^{-4}$, which gave a good, and fast convergence of the code. The final converged solution was set on an equidistant grid of 501×501 elements. Because this code was only suited for constant Ω_F a number of extensions had to be added in order to successfully solve Eq. 2.29 including the differential terms:

The first step was to add the differential term, $\tilde{\omega}\frac{\omega-\Omega_F}{\alpha}\Omega_F^{'}|\nabla\Psi|^2$, to the source term J (see Appendix A). The functions of $\Omega(\Psi)$ and $I(\Psi)$ were obtained by making a spline fit of the $\Psi(x)$ and $\Omega(x)$ and also for $I(x)$. This had to be done, because the functions $\Omega(x)$ and also for $I(x)$ had were a result of numerical integration (see §3.2.3) and should be calculated in the code for arbitrary $0 < \Psi < 1$. This spline also gave their derivatives with respect to Ψ, $I'(\Psi)$ and $\Omega'_F(\Psi)$. The function Ω_F was normalized by

choosing the asymptotic light cylinder radius. This gives the normalization factor $f_\Omega = 1/x_{\rm lc}$. In Appendix A it is shown how the $|\nabla\Psi|^2$ term was calculated. Because the Ω_F is also present in the l. h. s. of Eq. 2.29 the same spline procedure had to be applied there as well.

The second step was to include the iteration procedure of the position of the light surface. The first guess of the boundary for the light surface was initially made by calculating the light surface for constant $\Omega_F = 1/x_{\rm lc}$, because this corresponds to the maximal possible Ω_F of the light surface by definition (see Section 3.6.1). It turned out that for the non-constant rotation profiles the initial choice of the boundary gave problems when chosen too close to the light surface. Due to the initial choice of the boundary no convergence of the solution on this grid could be obtained. This was probably due to the fact that at the top, the boundary was, relative to the bottom, too close to the real light surface, which gave too little room for readjustment of the boundary during the iteration procedure. To solve this the initial boundary was shifted by an amount of $\Delta x_{\rm i} = 0.01 x_{\rm lc}$ inside, to be sure that the whole boundary is well inside of the light surface. This method proved to be successful. After each converged solution, for a given grid, for each cell at the boundary corresponding to the light surface, the value for $D(r,\theta)$ was calculated by

$$D(r,\theta) = 1 - \left(\tilde{\omega}(r,\theta)\left[\Omega_F\left(\Psi(r,\theta)\right) - \omega(r,\theta)\right]/\alpha(r,\theta)\right)^2 \qquad (4.1)$$

Each element at the light surface was shifted by $\Delta x = f_\Delta D(x,y)$. Here f_Δ was a chosen factor that could be adapted during the calculation in order to speed up the light surface iteration. It turned out that a good and fast convergence was obtained by choosing f_Δ as such that the amount of change was about 10% of the $D(r,\theta)$. After the shift of the outer elements, the internal grid was rearranged as well, and then the converged solution of the previous step was used as an initial condition for the calculation of the new $\Psi(r,\theta)$. For constant rotation, the number of iteration steps was about 10-20 in order to obtain a convergence of $\epsilon_{\rm conv} = 1\ 10^{-4}$. The initial few iteration over the new light surface took the same amount of steps, but gradually decreased to 2-3 steps to get the same convergence. This was because when the increment gets smaller, as the boundary approaches the real light surface, the converged solution on the previous grid will be much closer to the real final solution. The light surface iteration was stopped once $D(x,y)_{\rm max} < 1\ 10^{-4}$.

We encountered an unexpected problem when matching the 1-D solution of the asymptotic GSE to the upper boundary condition. The height of the grid was taken $5x_{\rm lc}$ for the jets calculated in the next sections, where the asymptotic light radius was chosen $x_{\rm lc} = 10\ {\rm R_g}$. The Kerr metric has three parameters of influence in the GSE, the red-shift $\alpha\left(r,\theta\right)$, the frame-dragging $\omega\left(r,\theta\right)$ and the $\tilde{\omega}\left(r,\theta\right)$. In the special relativistic regime far away from the black hole, the first reduces to 1, the second to 0, and the third is equal to the R-component in a cylindrical coordinate system. The values for the Kerr parameters for different heights in terms of the asymptotic light cylinder radius $x_{\rm lc}$ are given in Table 4.1.

height $(x_{\rm lc})$	$\alpha\left(r_{\rm lc},\theta_{\rm lc}\right)$	$\omega\left(r_{\rm lc},\theta_{\rm lc}\right)$	$\tilde{\omega}\left(r_{\rm lc},\theta_{\rm lc}\right)$	$x_{lc}\,({\rm R_g})$
5.00	0.9798	$1.2825\ 10^{-5}$	9.7991	9.7978
10.00	0.9899	$1.6249\ 10^{-6}$	9.8991	9.8988
15.00	0.9933	$4.8054\ 10^{-7}$	9.9329	9.9327
20.00	0.9949	$2.0229\ 10^{-7}$	9.9497	9.9496
∞	1.0	0.0	10.0	10.00

Table 4.1: Values for Kerr parameters at different heights of the grid (for $x_{\rm lc,\infty} = 10\ {\rm R_g}$)

At a height of $5x_{\rm lc} = 50\ {\rm R_G}$ the light surface has is at a distance of $x_{\rm lc} = 9.7978\ {\rm R_g}$ and has not yet reached its asymptotic value at $x_{\rm lc,\infty} = 10.0\ {\rm R_g}$. The Table 4.1 shows that the Kerr parameters have not reached their asymptotic values at this height. The question now arises whether the asymptotic solution, which has been calculated in the special relativistic regime, may be used as a valid boundary condition for the problem calculated in the Kerr metric. There are two options how to interpret the asymptotic solution. The first is to assume that both in the non-asymptotic region as well as in the asymptotic region the field is perfectly collimated. This, however, leads to some problems at the light surface. As can be seen in Fig. 4.1 that the flux surfaces that originally crossed the light surface (at the point where $x\Omega_F\left(\Psi\left(x\right)\right) = 1$), now cross it back. This is a contradiction, because $\Omega_F\left(\Psi\right)$ is conserved, so it cannot possibly cross the light surface a second time. Therefore all the flux that is outside the light surface must stay outside the light surface. It would be obvious to increase the height of the grid until the influence of the black hole becomes negligible. Because the grid cells should not get too elongated, to avoid numerical problems, we can

not set our boundary at arbitrarily high Z. For these we chose to normalize the asymptotic solution with respect to the position of the light surface at the top of our grid and not its asymptotic value. Because the difference of this point to the asymptotic value is very small (less than 2%), the difference between the asymptotically normalized jet and our adopted normalization should be insignificant. This does not mean that the solution becomes less accurate, it just implies a different rotation at the disk for some Ψ^*.

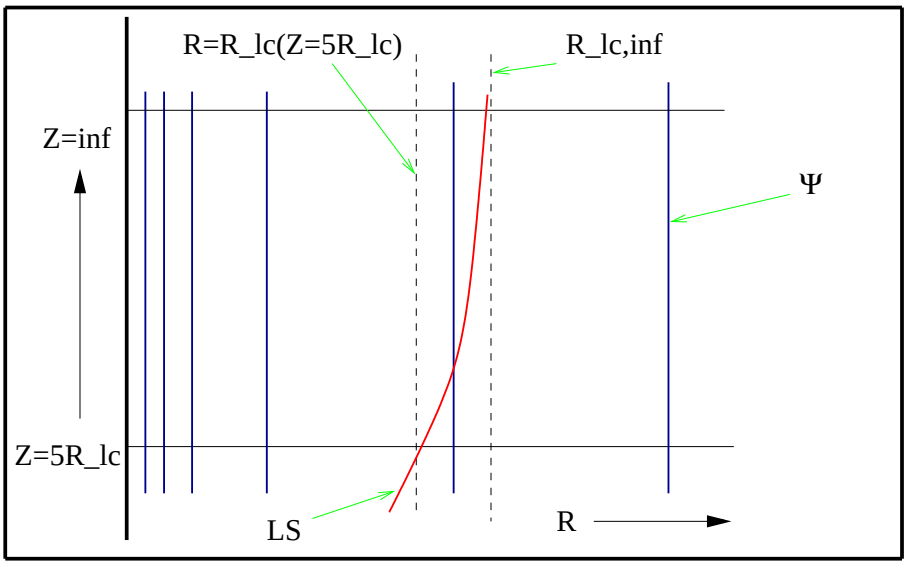

Figure 4.1: A schematic view of the problem when applying the asymptotic distribution as a boundary condition to a region where the light surface has not yet reached its asymptotic value. The assumed straight flux field will cross the light surface for a second time, which is in contradiction with $x\Omega_F(x) = 1$. The collimated flux surfaces (blue) and the light surface (red) are indicated in this figure. Note how in between the light surface and its asymptotic value the assumed collimated field lines may re-cross the light surface.

4.2 Testing the code

To test the extended new code was applied it to the case of constant rotation and differential rotation of the flux-fields.

In order to obtain the consistent solution, we adopted the the model parameters in a specific order. First an opening angle θ_0 was chosen because this parameter seemed to have to largest influence on the global structure. This determined the internal solution. By assuming some outer boundary by choosing the parameters $Z_{\rm yso}$, $f_{\rm yso}$, dR and n it was immediately apparent whether the g_I would have a possible 2-D solution with this opening angle. When an opening angle was found that had a solution for which the outer boundary gave an almost consistent solution, the opening angle was kept and the outer solution was changed until a consistent solution was found.

4.2.1 Constant rotation

In the case of constant rotation of the flux surfaces the analytical solution of Appl & Camenzind (1992) was used for the asymptotic boundary condition in order to solve the 2-D GSE. The asymptotic form of the GSE has, with the Ansatz that $I(\Psi) = \frac{1-e^{-b\Psi}}{1-e^{-b}}$, the analytical solution $\Psi(x) = 1/b \log\left(1 + \left(\frac{x}{a}\right)^2\right)$. The jet radius is then defined as $x_{\rm jet} = a\sqrt{e^b - 1}$. The parameters used originally by F1997a are given in Table 4.2. These were used to re-calculate structure as found by F1997a. Unfortunately the parameters describing the outer jet boundary used by F1997a were not specified in the paper, so we had to look for the solution again.

g_I	a	b	$r_{\rm lc,\infty}$	$\Psi_{\rm BH}$
2.14	2.71	0.8	10	0.2

Table 4.2: Jet model parameters as calculated by F1997a.

An initial guess of the jet boundary is done by taking a initial θ_0 the same as F1997a, which was about $\theta_0 = 3/4$ rad $\approx 42^{\rm o}$. The internal solution shown in Fig. 4.2.

To illustrate the method how the correct outer boundary was found two solutions for different boundaries are shown in Fig. 4.3. Both figures show clearly what happens if the outer boundary (as was shown in Fig. 3.11) is too different from the boundary that satisfies the internal force-balance. When the boundary is moved more inwards (collimates more slowly) the kinks move upwards. If the boundary is moved outwards, the kinks move downwards. The smooth solution where the derivatives of the flux distributions in the

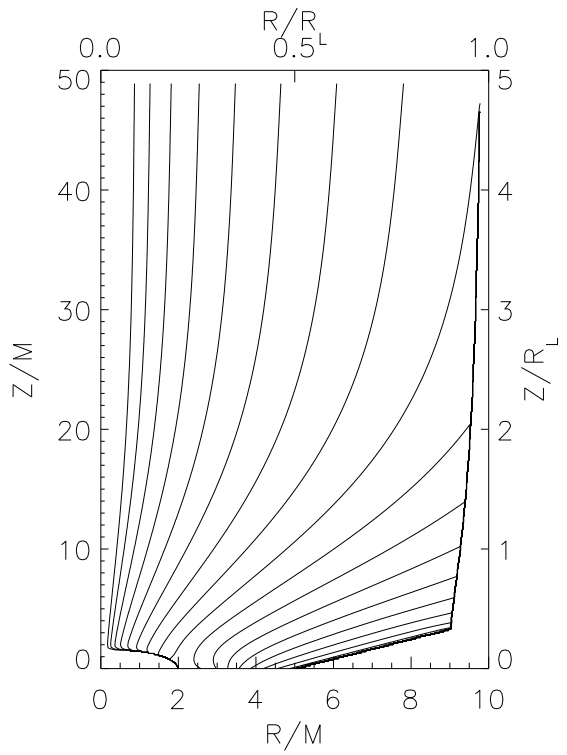

Figure 4.2: The inner region as calculated for the parameters of F1997a, with an opening angle of $\theta_0 = 42^o$. The contour lines indicate the values for $\Psi = 10^{-(0.1n)^2}$, with $n = 1, 2, ..17$.

inner region and the outer are equal, must have a boundary that is somewhere in between these boundaries.

In Fig. 4.4 can be seen what happens when the opening angle θ_0 is changed. Although the uniqueness of a this boundary is difficult to quantify, practice shows that when a given opening angle and outer boundary causing these kinks, these kinks can only be removed for one opening angle. In the left of Fig. 4.4, when the boundary is changed inwards (because now the kinks are downwards), the upper part of the distribution may become smooth, but the lower part still has a large kink. By doing this for a range in opening angles, it was found that fo too high opening angle we had this problem with upwards bending kinks, and for too low opening angles we had this problem with downwards bending kinks. A smooth transition at the light

surface could be found for the intermediate opening angle. The matching of the light surface was done by hand, which is quiet unsatisfactory, although it does give good results. An iterative procedure could be made by matchin the derivatives of the distribution at the light surface, although it will be very slow, because iteration would be needed over the outer boundary as well as the opening angle.

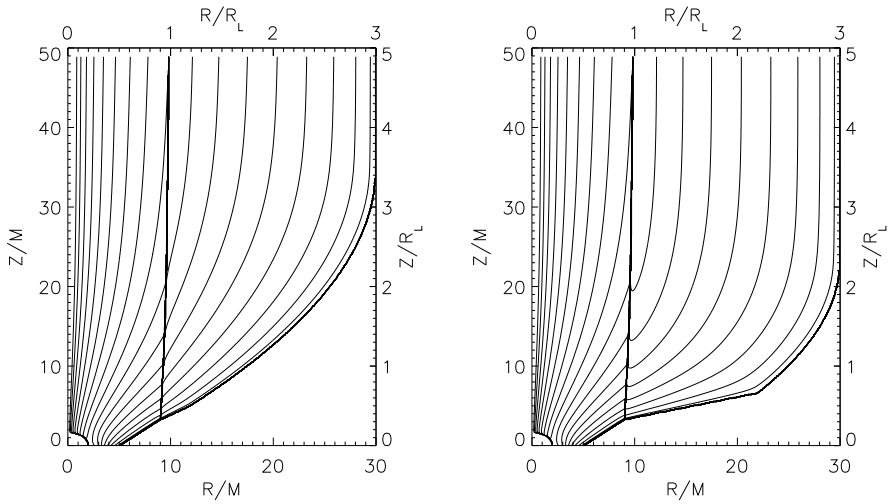

Figure 4.3: The inner region as calculated for the parameters of F1997a, with an opening angle of $\theta_0 = 42^o$. The contour lines indicate the values for $\Psi = 10^{-(0.1n)^2}$, with $n = 1, 2, ..17$. On the left: The parameters describing the outer boundary were $\theta_0 = 42^o$, $Z_{\rm yso} = 1.5 Z_{\rm ls,min}$, $f_{\rm yso} = 6.5$, $dR = 0.0007$ and $n = 2$. On the right: The parameters describing the outer boundary were $\theta_0 = 42^o$, $Z_{\rm yso} = 1.5 Z_{\rm ls,min}$, $f_{\rm yso} = 3.5$, $dR = 0.0008$ and $n = 2$.

The boundary that shows the best match at the light surface is shown in Fig. 4.5. The two shapes of the outer boundary are almost identical and the internal solution looks consistent. Due to the constant rotation, the position of the light surface is known in advance. The difference in the approach here, is that the whole 2-D structure, inside as well as outside the light surface at the same time was calculated by F1997a. The outer part was calculated separately and then matched to the inner part, because it had to be suited for finding the light surface of a differential rotation as well.

The solution seem very alike. Although the boundary may not be the exact boundary satisfying the GSE, which probably would not have the bound-

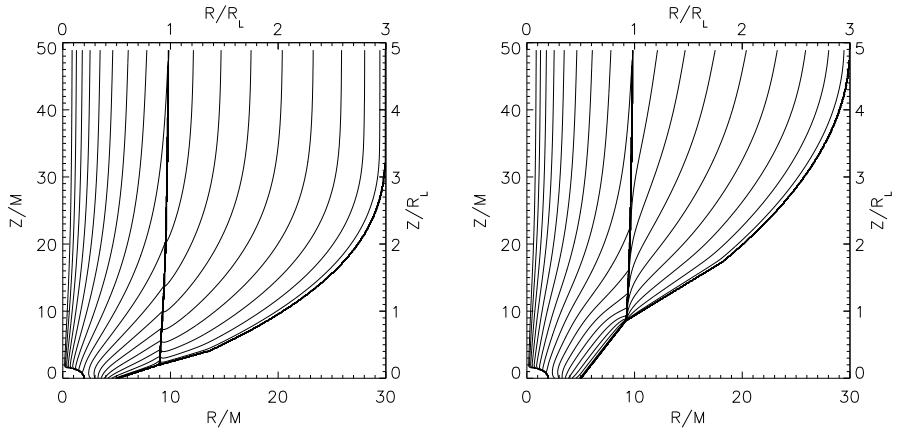

Figure 4.4: On the left: 2-D solution for higher opening angle than F1997a. The contour lines indicate the values for $\Psi = 10^{-(0.1n)^2}$, with $n = 1, 2, ..17$ (on the left) and $n = 1, .2, ..25$ (on the right). The parameters describing the outer boundary were $\theta_0 = 49.2^{\rm o}$, $Z_{\rm yso} = 2.0 Z_{\rm ls,min}$, $f_{\rm yso} = 8.4$, $dR = 0.000041$ and $n = 2.5$. On the right: The parameters describing the outer boundary were $\theta_0 = 32.7^{\rm o}$, $Z_{\rm yso} = 2.0 Z_{\rm ls,min}$, $f_{\rm yso} = 3.0$, $dR = 0.00018$ and $n = 2.0$. With these opening angles no outer boundary can be adopted, which gives a smooth transition at the light surface.

ary in a straight line at an opening angle θ_0 from the disk, the match at the light surface is so good the internal solution obtained with our approximate jet boundary will be close to that with the boundary that gives the exact solution of the GSE. In any case, the code was able to replicate the solution by F1997a up to a good degree of accuracy. The accuracy of the code with respect to the exact solution of the GSE will be discussed in § 5.1.

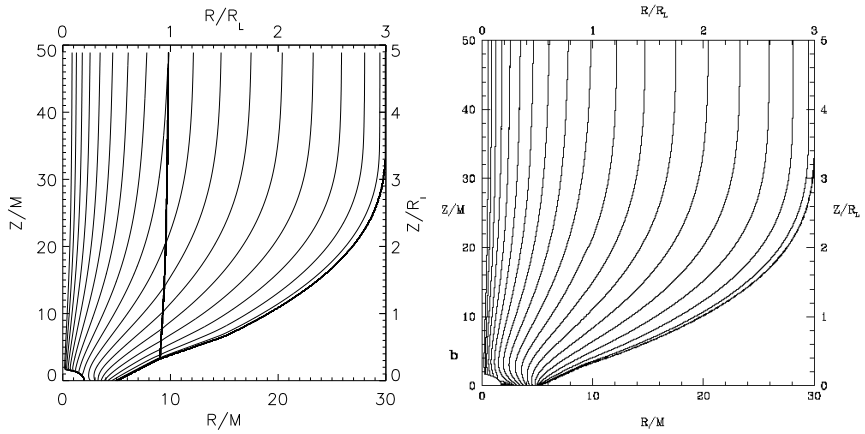

Figure 4.5: On the left: axisymmetric jet structure for constant Ω_F, as calculated with the new code. On the right: Same axisymmetric jet structure, as calculated by F1997a. The contour lines indicate the values for $\Psi = 10^{-(0.1n)^2}$, with $n = 1, 2, ..17$ (on the left) and $n = 1, .2, ..25$ (on the right). The parameters describing the outer boundary were $\theta_0 = 42^0$, $Z_{\rm yso} = 2.0 Z_{\rm ls,min}$, $f_{\rm yso} = 5.3$, $dR = 0.00038$ and $n = 2.5$. Note the difference near the disk, as F1997a took the boundary condition along the disk somewhat different $\Psi_{\rm disk} = E\Psi_{\rm max}\left(r - r_0\right)^n$ with $n = 3$, $r_0 = 1.76$ and $E = 0.03$. It can be seen that the disk boundary condition does not affect the global solution. This shows that for a constant rotation law, the new code successfully reproduces the solution as found by F1997a.

4.2.2 Differential rotation

In order to compare our results with the previous work by FM2001 where only the differential rotation of the flux surfaces was included the exponential rotation profile $\Omega_F^2\left(x\right) = \sqrt{e^{h-hx}}$ was chosen, with a steepness of $h = 0.2$. For the current density distribution $I\left(x\right) = \left(x/a\right)^2 / (1 + \left(x/a\right)^2$ was taken. The parameters used are given in Table 4.3. Because the solution obtained by FM2001 was normalized with respect to the asymptotic light cylinder, we had to re-normalize the asymptotic light cylinder radius in terms of the gravitational radius (as discussed in Section 3.2.4) to calculate the 2-D structure. For the test, the asymptotic radius was chosen at $x_{\rm lc} = 25$ $\mathrm{R_g}$, which gives with the disk size $r_{\rm disk} = 5$ $\mathrm{R_g}$ like F1997a the same light surface to disk size ratio as FM2001.

As initial opening angle $\theta_0 = 75^{\rm o}$ was chosen. The solution for the inner

g_I	a	h	$r_{\mathrm{lc},\infty}$	Ψ_{BH}
2.5	1.0	0.2	25.0	0.2

Table 4.3: Jet model parameters as calculated by FM2001.

region with the initial choice of the outer boundary are shown in Fig. 4.6. The initial inner solution was shifted 0.1 $\mathrm{R_g}$ to the left of the light surface for $\Omega_F = 1/r_{\mathrm{lc}} = 0.04$. It took 140 steps for the iteration procedure, which moves the outer boundary to the light surface, to converge to $D\left(x,y\right)_{\mathrm{max}} < 1\ 10^{-4}$. The combined solution for the inner and outer regions is shown in Fig. 4.7. The solution as calculated by FM2001 is shown in Fig. 4.8. Again the global solutions are very alike, as they are determined by the asymptotic free functions as found by F1997a. The solution near the disk differ however. This is for a part due to a different boundary condition taken along the disk and the central object. FM2001 took at the disk a distribution of

$$\Psi_{\mathrm{disk}}\left(x\right) = \frac{1}{\tilde{b}} \ln\left(1 + \left(\frac{x - x_{\mathrm{in}}}{\tilde{a}}\right)^2\right) \tag{4.2}$$

with $\tilde{a}$ the core radius of the flux at the disk and $\tilde{b} = \ln\left(1 + \left(x_{\mathrm{disk}} - x_{\mathrm{in}}\right)^2 / \tilde{a}^2\right)$. The second difference is the influence of the Kerr metric near the rotating black hole. The global solutions are the same as those determined by the asymptotic free functions as found by F1997a. The outer boundary is slightly different, but for the purpose of testing the combining of the two methods, this is quite satisfactory.

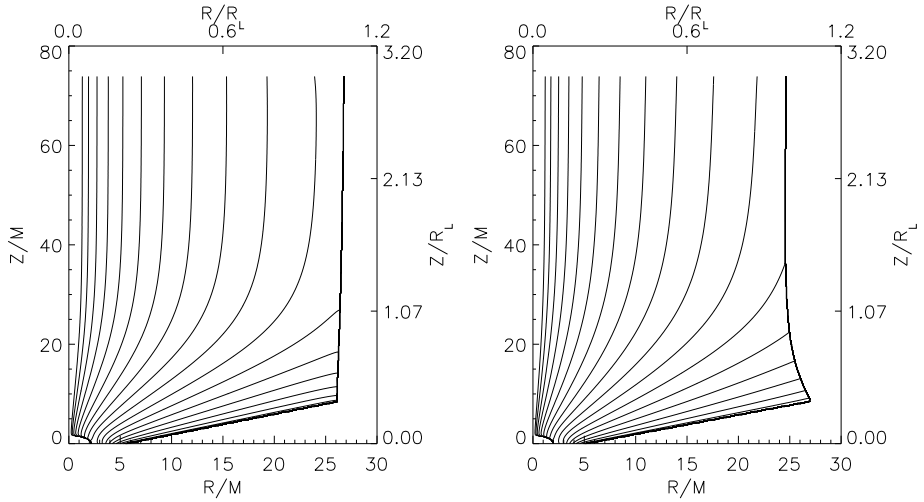

Figure 4.6: On the left: Converged solution for the initial choice of the outer boundary that was shifted 0.1 R_g inside of the light surface for $\Omega_F = 1/r_{lc} = 0.04$. The opening angle is $\theta_0 = 75^o$. On the right: The final inner solution after 140 iteration steps of the light surface. Both are for a steepness $h = 0.2$. The contour lines indicate the values for $\Psi = 10^{-(0.1n)^2}$, with $n = 1, 2, ..17$.

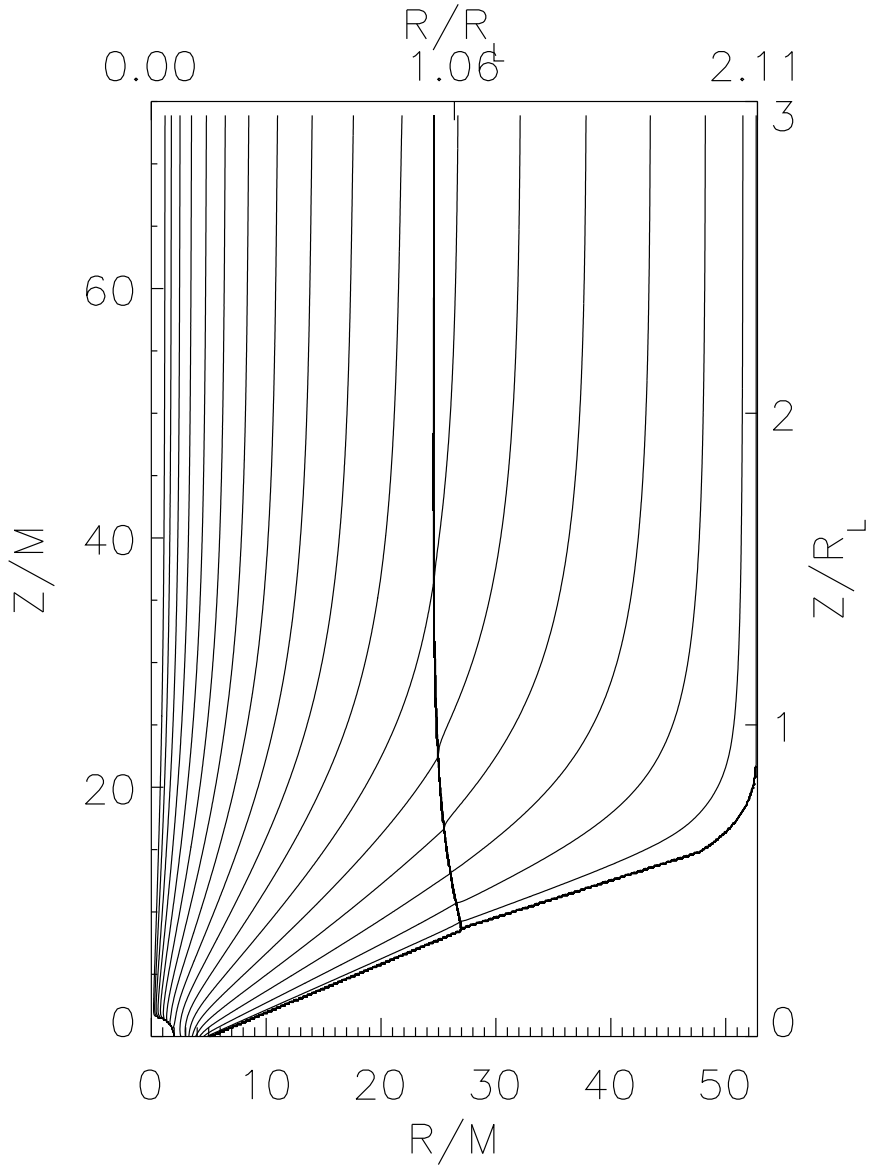

Figure 4.7: The axisymmetric jet structure for a *differentially* rotating flux-distribution with steepness $h = 0.2$, including the *Kerr metric*. The contour lines indicate the values for $\Psi = 10^{-(0.1n)^2}$, with $n = 1, 2, ..17$. The parameters describing the outer boundary were $\theta_0 = 75^{\rm o}$, $Z_{\rm yso} = 1.7 Z_{\rm ls,min}$, $f_{\rm yso} = 1.8$, $dR = 0.000091$ and $n = 3.0$.

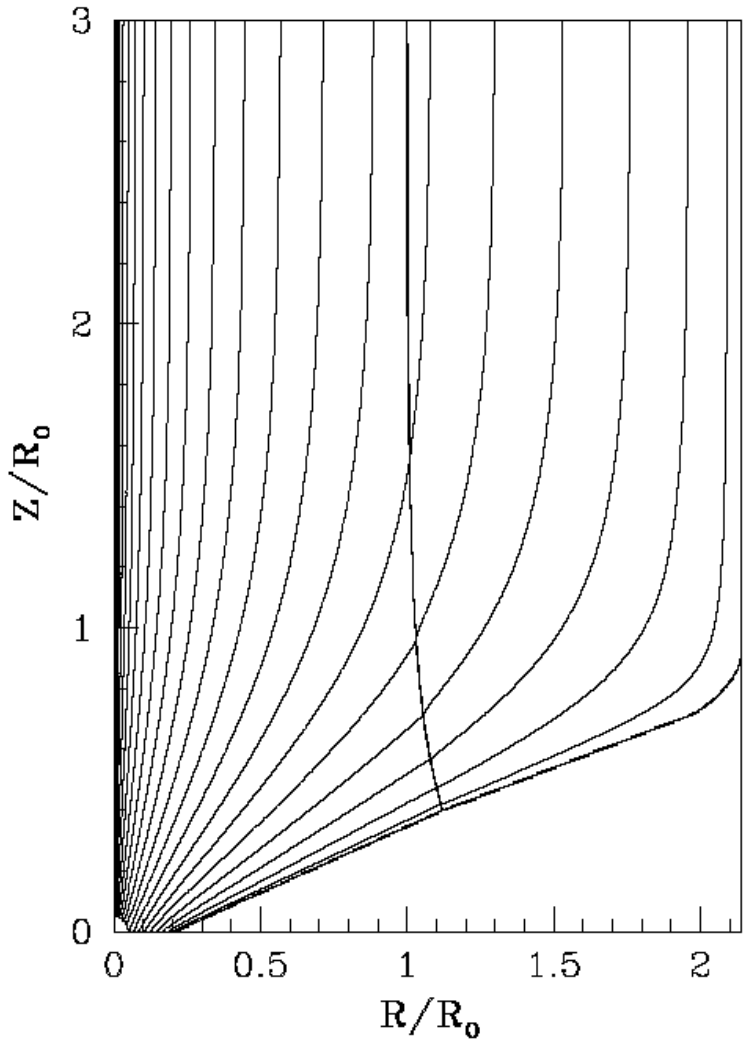

Figure 4.8: The axisymmetric jet structure for a *differentially* rotating flux-distribution jet structure, as calculated in a special relativistic treatment by FM2001. The contour lines indicate the values for $\Psi = 10^{-(0.1n)^2}$, with $n = 1, .2, ..25$ (on the right).

Chapter 5

Discussion & Future Work

5.1 Discussion

In calculating the force balance across the magnetic flux fields, the combination of the Kerr metric with the differential rotation of the field lines appears to be successful. In the case of constant rotation the same solution as calculated by F1997a was found. Because the outer boundary exact shape as found by F1997a was not conserved, we had to find the boundary again. We found a slightly different jet boundary than F1997a (see Fig. 4.5), but the solutions look almost exactly alike. What can be seen is that in the region near the disk the solutions differ somewhat. This is due to the slight difference in boundary conditions along the disk and the different boundary near the black hole. F1997a took the light surface as the inner boundary, we took the ergosphere. The global solution is not affected by the difference in boundary conditions at the disk. This is because both have the same free functions $I(\Psi)$ and $\Omega_F(\Psi$ as determined from the asymptotic analytical solutions of Appl & Camenzind (1993). Because the code was based on the code that calculated the same solution, so we expect no difference in the accuracy of the code. This is somewhat different in the case of replicating the solution of FM2001. By comparing the solution as found by our code with that of FM2001 we can say that we found almost the same solution. Although there are still some small kinks left at the light surface this approximate solution closely resembles that of FM2001. For testing the code, this result is good enough to be sure that the combination of the Kerr metric and the differential rotation has been successful.

Top-down approach and the rotation profile Ω_F The problems when adopting some rotation profile Ω_F in the top-down approach were described in Section 3.2.4. When trying to match this profile to some physical rotation profile the steepness (in our case $h = 0.2$) in combination with the coupling constant g_I was too small, based on arguments concerning the ratio of maximal and minimal rotation of the asymptotic rotation profile and the disk rotation profile. When the steepness was increased, this showed that the light surface returned in the asymptotic regime. A second problem, was that according to some arguments the rotation of the flux fields around the black hole's environment rotate at constant rotation at some fraction of the black hole's rotation $\Omega_F = f\Omega_{\rm BH}$ (Punsly 2001). Therefore an asymptotic rotation profile should have some cut-off value that corresponds to this rotation. We did some investigation with a modified rotation profile

for $x > x_{\rm bh}$

$$\Omega_F = \frac{e^{1/((x-x_{\rm bh})^n+f)}}{h\left(x-x_{\rm bh}\right)^m+1} \tag{5.1}$$

for $x \leq x_{\rm bh}$

$$\Omega_F = e^{1/f} \tag{5.2}$$

with $f = 1/\log\left(h\left(1-x_{\rm bh}\right)^m+1\right)-\left(1-x_{\rm bh}\right)^n$. Here $x_{\rm bh}$ is the position normalized in asymptotic light cylinder radii, where the rotation profile becomes constant. The parameters m, n can be chosen such that a high rotation is obtained inside the light cylinder and a low fall off for higher x, making sure that no returning light cylinder was close to the jet boundary. The same IDL procedure as used in Section 3.2.3 was used to solve the asymptotic GSE for this rotation profile (see Fig. 5.2).

The main drawback of this method was that yet more parameters $x_{\rm bh}, m, n$ had to be chosen, and for example $x_{\rm bh}$ is determined by the internal force balance. Also to obtain an exact match between a Keplerian profile and the asymptotic rotation profile while conserving $\Omega_F(\Psi)$ will always stay a problem while using the solution of the asymptotic jet to determine the internal structure. Although it must be stressed that the solutions, obtained with the top-down approach, do give exact solutions for the jet structure, for these reasons in Section 5.2 an alternative bottom-up approach will be explained and its advantages and disadvantages will be discussed.

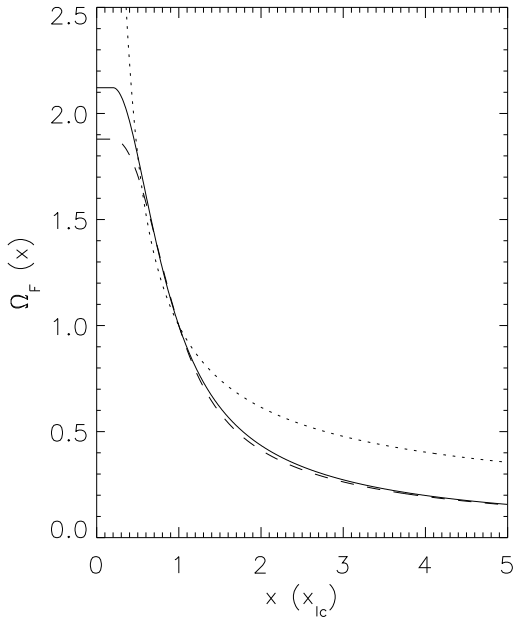

Figure 5.1: Profile for $\Omega_F(x)$ as in Eq. 5.1. For $x_{\rm bh} = 0.2$, and different (m, n): dotted (1,1), solid (2,2), striped (2,3).

Jet collimation Although the jet does not propagate through a vacuum, this is not necessary for collimation. When the electromagnetic pressure exceeds the ambient pressure the shape of the jet will not be affected. The pressure of the ambient confining medium spans a wide range, from values of 10^{-2} dyn cm^2 in the broad line region to 10^{-12} dyn cm^2 in the intergalactic medium (Appl & Camenzind 1993). The ambient pressure can be related to jet pressure. For a jet to be in equilibrium, the sum of stresses on the boundary inside and outside must cancel

$$\frac{1}{8\pi}\left(B_\phi^2 + B_P^2 - E_P^2\right)_{\rm jet} = P_{\rm ext} + \frac{1}{8\pi}B_{\phi,\rm ext}^2 \tag{5.3}$$

The dimensionless pressure can be expressed as $p = (R_{\rm LC}^4/\Psi_{\rm max}^2)\,P$ which has the units

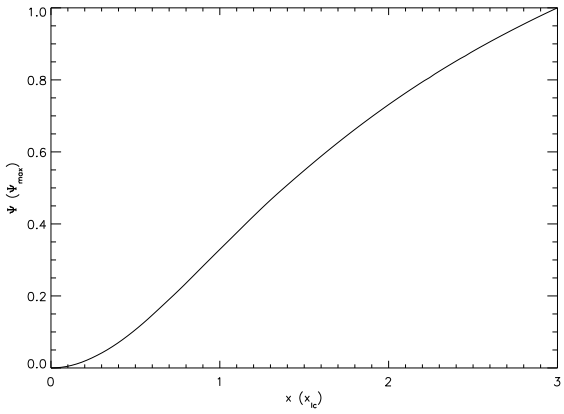

Figure 5.2: Asymptotic flux distribution as calculated for rotation profile as in Eq. 5.1. Here $a = 1$, $B = 1$, $h = 0.2$, $x_{\rm jet} = 0.2$, $g_I = 1.97$ and $(m, n) = (2, 2)$.

$$p = \left(\frac{P}{10^{-6}\ \mathrm{dyn\ cm^{-2}}}\right)\left(\frac{R_{\rm LC}}{10^{15}\ \mathrm{cm}}\right)^{4}\left(\frac{\Psi_{\rm max}}{10^{33}\ \mathrm{G\ cm^{2}}}\right)^{-2} \tag{5.4}$$

The jet is defined by the set of nested flux surfaces with $0 \leq \Psi \leq 1$. This can be done for a saturating profile at $\Psi = 1$ because then there is no poloidal field left beyond this point ($d\Psi/dx = 0$). In principle, one can distinguish between two different regimes for a jet (Appl & Camenzind 1993): a current-confined (or self-confined) or a pressure-confined jet. Self-collimation is shown to be possible by time-dependent simulations for particular cases (Ouyed & Poudritz 1997), but the spatial scales were far below the scales of the collimating regime. There are also arguments based on current-closure that confinement cannot occur without external help (Okamoto 1997, 1999). For now we assume that the jet is current-confined and the external pressure can be neglected.

Possible follow-up studies may be done in order to include external gas pressure. A possible idea might be to make the pressure gradient as a function of the flux-fields $\nabla P\,(\Psi)$. Then it could be included as an extra term in the source term. It is not really clear what kind of function one then would take for the pressure distribution though. A constant external pressure and a zero pressure in the force-free jet would lead to an infinite high gradient at $\Psi = 1$, so one needs some idea on what to take for the gradient at the jet boundary.

Whether this can work or not still has to be investigated.

Jet stability Having found these solutions for the axisymmetric jet structure, the question arises whether they are stable or not. We have not found the time to address this problem yet, and this will have to be done in the future. Many studies have been done on the stability of stationary MHD jet solutions (e. g. Appl 1996; Lery 1996; Lery & Frank 2000) show that solutions for MHD jets, especially current carrying ones are more stable than hydrodynamic ones. The stability will probably depend on the type of current distribution $I(\Psi)$ (see Fig. 3.3). The current profile taken is a profile where most of the current is located inside the core radius a (in our solution in Section 4.2.2 $a = 1$, which corresponds to the asymptotic light cylinder) and then drops off for larger Ψ (a profile similar to what Khanna & Camenzind (1992) obtained for their stationary disk solutions). A parameter study of the core radius a, the coupling constant g_I will have to be done in order to see what effect they have on the jet structure and see whether it is indeed stable.

5.2 Calculating the flux structure from disk physics

The top-down approach used in this thesis, takes the asymptotic version of the GSE, to calculated the asymptotic boundary condition used by the 2-D GSE. To solve this, for the current distribution $I(\Psi)$ and for the rotation profile $\Omega_F(\Psi)$ assumption had to be made. The top-down approach uses the results of studies made by Appl & Camenzind (1993) and F1997b of the asymptotic special relativistic GSE which assumes some current-distribution and rotation profile as a function of x (in terms of the asymptotic light cylinder radius $x_{\rm lc}$). From these functions then a consistent solution for the asymptotic GSE can be calculated. This can give some complications, however, when trying to match these functions to the physical properties, such as the rotation of the magnetic fields at the disk. An alternative bottom-up approach would be to base the distributions of $\Psi(x)$, $I(x)$ and $\Omega_F(x)$ on the physical properties of the disk and around the black hole, which can be based on calculations done by for example Khanna & Camenzind (1992), Okamoto (1992) and others. When one has these descriptions of these three distribu-

tions, one also has the functions $\Omega_F(\Psi)$ and $I(\Psi)$ which are needed to solve the 2-D GSE. The question is now, how to find the appropriate asymptotic boundary condition. As already mentioned in Section 3.2.2, when we have the situation that there is no returning light surface into the asymptotic region, the light surface can be used as a boundary condition for calculating the structure inside the light surface. In our approach, for this region the asymptotic Dirichlet boundary condition is not mandatory. A homogeneous Neumann boundary condition (e. g. fully collimated field lines) is enough. The problem is that the position of the outer boundary in the asymptotic region $x_{\rm jet}$ is now unknown, because we only have $\Omega_F(\Psi)$ and $I(\Psi)$ and not $I(x)$ and $\Omega_F(x)$ which can be used to integrate the asymptotic GSE. We now start with the rotation profile normalized in the dimension of the Kerr metric, but the true scaling is a result of the internal solution that we want to calculate (as discussed in Section 3.2.4). In Section 4.1 we showed the possibility of starting inside of the light surface and use an iterative procedure to find it. It could therefore be possible, to start at a low position and use the same procedure to find the unknown light surface and with it the correct scaling of the asymptotic light cylinder radius. The regularity condition at the light surface will make sure this is possible. It is not as straightforward to find a solution for the region outside of the light surface, because the position of the jet outer boundary is not known in advance either.

We propose a method to find the boundary by solving the 2-D GSE in the asymptotic regime with our code. Because the scaling of the asymptotic light surface can be found, the exact position is known and we can try to find the true solution by varying the outer boundary where $\Psi = 1$.

As a first test of this idea we used the analytical solution of Appl & Camenzind (1992) for $\Psi(x)$ and the adopted $I(x)$ and $\Omega_F(x)$ to get the functions for $I(\Psi)$ and $\Omega_F(\Psi)$. Because the real solution is known by integrating the asymptotic equation, we can examine how the solution changes when a different $x_{\rm jet}(\Psi = 1)$ is taken. We used a rectangular grid far from the black hole, so that the light surface becomes a cylinder. We chose only Dirichlet boundary conditions at the inner part $\Psi(x) = 0$ and at the boundary $\Psi(x_{\rm jet}) = 1$, and chose the scaling of the asymptotic light surface of $x_{\rm lc} = 100\ {\rm R_g}$ which gives a jet radius of $x_{\rm AC,jet} = 213.80\ {\rm R_g}$. We do not set the boundary conditions at the top and bottom of the grid! In Fig. 5.3 the solutions are shown for the $x_{\rm jet} = x_{\rm AC,jet} - 5, x_{\rm AC,jet}$ and $x_{\rm AC,jet} + 30$. No converging solution could be obtained for $x_{\rm jet} = x_{\rm AC,jet} - 10, x_{\rm AC,jet} + 50$.

From Fig. 5.3 it can be seen that for the boundary taken at $x_{\rm AC,jet}$ the

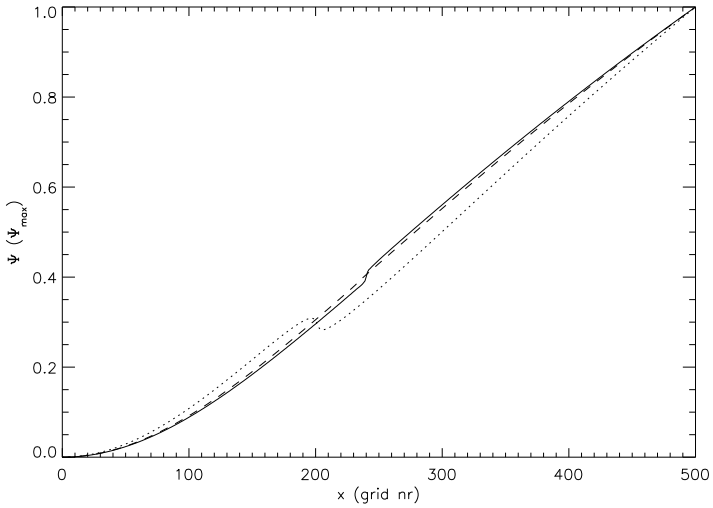

Figure 5.3: Solutions for the 2-D GSE by varying the boundary of the jet $x_{\rm jet}$. The dashed line indicates the jet with the boundary $x_{\rm AC,jet}$, the dotted line with $x_{\rm AC,jet} - 5$ and the solid line with $x_{\rm AC,jet} + 30$. Because the solutions are plotted against the equidistant grid points, the asymptotic light cylinders are not on the same position in the plots. It is clear that kinks appear around the asymptotic light cylinders for the boundaries that do not correspond to $x_{\rm AC,jet}$.

same solution is obtained as that from the integration. For small deviation from $x_{\rm AC,jet}$ a kink $d^2\Psi/dx^2 = 0$ appears around the asymptotic light cylinder. For larger deviations the code did not converge at all. The solution only converged for smaller $x_{\rm jet} < x_{\rm AC,jet}$ for smaller deviations than for $x_{\rm jet} > x_{\rm AC,jet}$. The maximum deviation was about 10% of the jet radius for $x_{\rm jet} > x_{\rm AC,jet}$ and about 2% for $x_{\rm jet} < x_{\rm AC,jet}$. The direction of the bump changes as well when $x_{\rm AC,jet}$ is passed, which might be an indication for the correct solution.

Although care should be taken in over interpreting these results, it is an indication that the boundary may be found by examining the behavior of the converged solutions around the light cylinder. This may be done by starting to take the value of $x_{\rm jet}$ from the light surface and increase the value in small steps, and look for converged solutions. The true solution must lie in between the point where the kinks change sign. It is still unclear how accurate this method might be to obtain the exact solution. Whether this holds for an

arbitrary $I(\Psi)$ and $\Omega_F(\Psi)$ is also still unclear. This has to be studied more extensively.

In order to use the bottom-up approach the full distributions of $\Omega_F(x)$, $I(x)$ and $\Psi(x)$ have to be specified for the black hole/accretion disk system. Although there have been some studies of this, a fully consistent disk model has not yet been found. Because in the bottom-up approach the jet structure is determined mainly by these quantities, this might be a useful method also to test disk models. It could be seen that for different disk boundary conditions, the same global solution was obtained. Because the top-down approach uses the asymptotically determined free function, this is expected. It would be interesting to study how the disk physics will influence the global solution for the bottom-up approach, because in this case, the whole axisymmetric solution is entirely determined by it and not only locally as in the top-down approach.

5.3 Solving the energy equation along the flux surfaces

With the calculated magnetic flux distribution that was obtained solving the cross-field force balance it is now possible to calculate the flow properties along the flux surfaces, which gives for example the final flow of the accelerated plasma. These follow from the force-balance along the field lines, called the Wind Equation (also known as the Bernoulli Equation), which represents the integrated stationary MHD energy equation. The most general version of the stationary relativistic wind equation (Camenzind 1986; Takahashi et al. 1990) is given in terms of the relativistically defined poloidal velocity $u_p \equiv \gamma v_p/c$ by

$$u_p^2 + 1 = -\sigma_m \left(\frac{E}{\mu}\right)^2 \frac{k_0 k_2 + \sigma_m 2 k_2 M_A^4}{\left(k_0 + \sigma_m M_A^2\right)^2} \tag{5.5}$$

with $k_0 = g_{33}\Omega_F^2 + 2g_{03}\Omega_F + g_{00}$, $k_2 = 1 - \Omega_F \frac{L}{E}$, and

$$k_4 = -\frac{g_{33} + 2g_{03}L/E + g_{00}L^2/E^2}{g_{03}^2 - g_{00}g_{33}}$$

Fendt & Camenzind (1996) did these calculations for a calculated flux distribution for constant rotation to study the influence of the magnetization σ_m on various parameters of the flow (see Fig. 5.4). It would be interesting to study the influence of the Kerr metric and the differential rotation on these parameters.

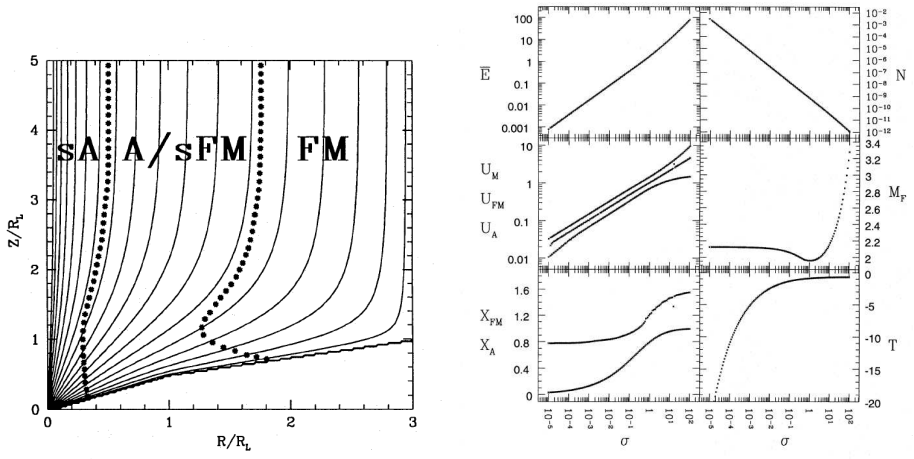

Figure 5.4: On the left: Overall structure of the critical surfaces of the collimated jet. The regions indicated are the sub-Alfvénic (sA), super-Alfvénic, but sub-fastmagnetosonic(A/sFM), and super-fastmagnetosonic (FM) (taken from Fendt & Camenzind 1996). On the right: The dynamical parameters along the flux surface $\Psi = 0.726$ for various degrees of magnetization σ_m. The dynamical properties are the total energy minus the rest energy $\bar{E} = E(\Psi) - 1$, the maximal poloidal velocity near the asymptotic radius, u_M, the poloidal velocity near the fast magnetosoinc point u_F, and the Alfvén point u_A. Also the positions of the fas magnetosonic point x_{FM} and the Alfvénic point x_A. The particle density N in cm^{-3} at the position of u_M. Fast magnetosonic Mach number M, and the poloidal current T, in units of $\Psi_{\max}/R_L$ (taken from Fendt & Camenzind 1996).

Although $\Omega_F(\Psi)$ is conserved even in a non-force-free plasma (as it follows from the axisymmetry assumption), $I(\Psi)$ is not. In order to calculate the dynamics of the stream the force-free assumption has to be dropped, because the inertial terms are essential to get the acceleration of the flow. The approach is therefore not entirely consistent. To do it really consistently, an iteration over the current distribution should be adopted: A initial current distribution is taken and a force-free calculation of the cross-field balance

is done. That field distribution is used to calculate the force balance along the fields including inertial terms, which gives a new current distribution. Of course the question whether such an iteration iteration would converge should be investigated, and because it is probably very time-consuming and maybe as a good approximation it may be left out, especially for highly magnetized flows. This must investigated further.

5.4 Polarization of the jet synchrotron emission

Another interesting follow-up from the work done, is the possibility to calculate the synchrotron polarization from radio emission. Pariev, Istomin and Beresnyak (2003) recently published their calculations for the degree of polarization of synchrotron emission in force-free MHD jets. They assumed a simplified model for the structure and the rotation profile of the fully collimated magnetic flux surfaces (see Fig.5.5).

Their adopted rotation profile was

$$\Omega_F = \Omega \frac{c}{R}\left(1 - \left(\frac{r}{R}\right)^2\right) \tag{5.6}$$

With Ω the dimensionless strength of the rotation, and R the boundary of the jet. The Stokes parameters for their configurations were given by

$$I = \frac{\zeta + 7/3}{\zeta + 1} k(\nu) \int_0^R dh \int_{\phi_1}^{\phi_2} |B_\perp|^{(\zeta+1)/2} \frac{h}{\sin\theta \sin^2\phi} d\phi \tag{5.7}$$

$$Q = k(\nu) \int_0^R dh \cdot \int_{\phi_1}^{\phi_2} |B_\perp|^{(\zeta-3)/2} \frac{[\Omega_F^2 r^2 \cos^2\phi - (c\sin\theta + \Omega_F r \sin\phi \sin\theta)^2] B_z^2 h}{c^2 \sin\theta \sin^2\phi} d\phi \tag{5.8}$$

$$U = V = 0 \tag{5.9}$$

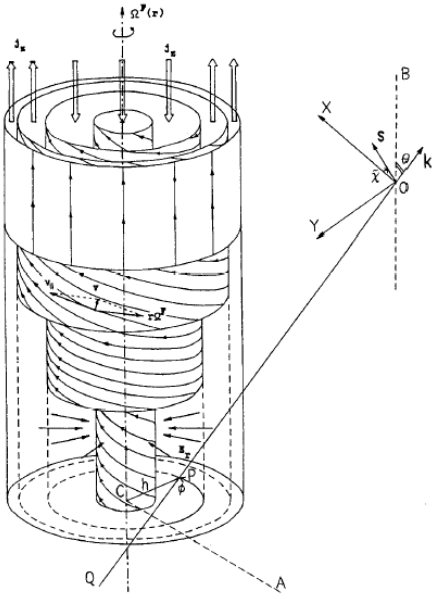

Figure 5.5: Structure adopted by Pariev et al. (2003) for their calculations of the polarization of synchrotron emission in collimated jets (taken from Pariev et al. 2003).

They found that the strength of the rotation Ω has a strong influence on the degree of polarization of the synchrotron emission (see Fig. 5.6). Their adopted structure and rotation profile however do not satisfy the cross-field force balance. What would be interesting is to redo these calculations using the flux surface distributions calculated by the method presented in this thesis. Then from the rotation law of the disk, a more consistent calculation can be done for the degree of polarization of the synchrotron emission. We cannot directly compare our results to the work of Pariev, Istomin and Beresnyak (2003) and predict the polarization as expected using our solution, because in their paper they assume constant B_z and a different rotation profile while doing the derivation and their presented equations are not immediately applicable to our obtained solutions. When this is done the calculated emission might be a useful tool to probe the collimation region of the jet.

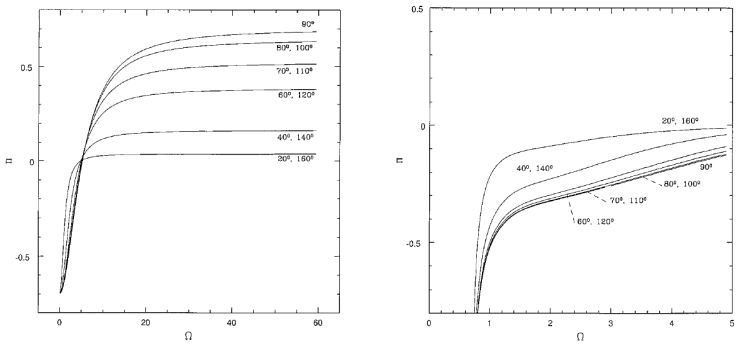

Figure 5.6: Dependence of linear polarization Π on the strength of the angular rotational velocity of the magnetic flux surfaces and different angles of view. On the left: For a homogeneous distribution of emitting particles. On the right: For emitting particles concetrated close to the Alfvénic resonance surface (both taken from Pariev et al. 2003)

Chapter 6

Conclusion

In this thesis I studied the force-free force balance across the surfaces of constant magnetic flux in collimating relativistic jets with the inclusion of the differentially rotating term of the magnetic field structure in a background of the Kerr metric of the central black hole. The focus was primarily on the problems encountered when combining the separate studies done by F1997a on the Kerr metric, and FM2001 who included the differential term in a special relativistic treatment. The advantage of this combination is the possibility of consistently matching the calculated structure of the collimated jet to physical properties of the disk and the central black hole. Also the influence of the metric on the electromagnetic fields is consistently incorporated in this treatment. For this thesis the code that calculated the force-balance in a Kerr metric using a finite element approach was extended to include the differential rotation of the magnetic field lines. The calculations done by the resulting code were compared to those done by F1997a and FM2001. These tests out that the new code can successfully obtain the same results. The solution shown in Fig.4.7 is therefore a full solution that includes the differential rotation of the flux surfaces and the general relativistic description of the space-time.

In order to solve the GSE the free functions of the the differential rotation profile $\Omega_F(\Psi)$ and $I(\Psi)$ had to be specified. We did this according to a top-down approach as adopted by FM2001, which uses the analytical studies of asymptotically collimated jets done by Appl & Camenzind (1993) and F1997b to obtain the free-functions $\Omega_F(\Psi)$ and $I(\Psi)$. These were then used to calculate the global solution by solving the axisymmetric GSE.

By studying the asymptotic GSE, we found the possibility for a relativistic

core structure in the asymptotic collimated jet. For some rotation profiles, the light surface (the Alfvénic surface in the case of high magnetization) can return into the asymptotic regime, thereby dividing the jet into an inner sub-relativistic part, a relativistic core, and an outer sub-relativistic envelope. As far as we know, this has not been mentioned yet in previous studies on asymptotically collimated jets. It does resemble the super-Alfénic core Casse & Keppens (2002) see in their time-dependent non-relativistic simulations. Up till now, studies of relativistic jets have been concerned only with jets having an inner sub-relativistic region and an outer relativistic envelope. Due to the extra complexity of the relativistic core structure, we do not yet treat these structures with returning light surface.

Although this approach did give a consistent solution to Eq. 2.29, it presented some problems when trying to match the structure to the disk/black hole physics. For some disk models that imply some distributions $\Omega_F(x)$, $I(x)$ and $\Psi(x)$ to find the jet-structure that fits these distribution, the top-down approach did not give a direct match, because it was not clear what asymptotic distributions to take for the asymptotic rotation profile $\Omega_{F\infty}(x)$. The rotation profile as used for the solution in Fig. 4.7 is too flat to match a Keplerian rotation at the disk.

An alternative bottom-up approach was introduced to solve the axisymmetric structure by starting from the disk distributions instead of the asymptotic distributions. Instead of determining the free functions $\Omega_F(\Psi)$ and $I(\Psi)$ from the asymptotic regime, these were taken from the disk/black hole physics itself. The rotation profile in combination with the flux distribution gives the formal asymptotic light surface for any flux Ψ^*. Whether this flux collimates at the light surface is a result of the 2-D solution. We showed that the light surface could successfully be obtained when starting out inside of the surface and then shift the boundary outwards bit-by-bit, which was possible due to the regularity condition at the light surface. Therefore it should be possible to obtain the light surface. Instead of now solving the asymptotic version of the GSE, we propose to solve a asymptotic version of the 2-D GSE using the newly developed code. The only unknown is the outer boundary position $x_{\rm jet}$. By varying the boundary $x_{\rm jet}(\Psi = 1)$ there are indications that the solution can be found by these means. Because there was too little time to fully study this approach, more extensive work is needed. The asymptotic solution obtained in this way can then be used to calculate the global solution as done by FM2001. The bottom-up approach would then give a consistent match between the jet structure and the black hole/accretion disk

boundary conditions. The bottom-up approach may also show out whether the rotation profile at the disk will have a relativistic core structure or a relativistic envelope structure. Possible follow-up studies were discussed were the solution obtained with the newly developed code could be used in order to solve the force-balance along the field lines, allowing for estimations of the final velocities of the plasma. Also the solutions give the possibility to calculate the polarization of the jet emission. In future work the stability of our solutions also has to be examined. Also a parameter study has to be done for various parameters like the coupling constant g_I, and the core radius a of the current distribution.

We realize that the many assumptions (stationarity, axisymmetry, force-freeness, full collimation of the asymptotic jet) may weaken our treatment of the jet structure, although reasonable arguments have been given to justify them, but we note that for the moment these kind of treatments are the only possible way to treat the jet in a *global* sense. This is needed in order to learn from the global jet structure the internal processes that are yet (and will remain) unobservable. To fully understand how the jet is initiated, collimates and propagates, a time-dependent study that includes the disk, central object and the environment in a consistent way is inevitable, but for objects as complex as relativistic jets this is still far away for now.

Acknowledgements

First of all I would especially like to thank Christian Fendt for having given me the opportunity to do the research for my master thesis with him and for all the interesting and fruitful discussions we had during the nine months that I spent in Potsdam. I would like to thank the 'Astrophysikalisches Institut Potsdam' (AIP, Potsdam) for giving me the time and space for doing my research at the institute. Further I would like to thank the 'traveling fund' of faculty Mathematics and Natural Sciences (Leiden), the 'Curatorenfondsen' and the 'J. C. Kapteynfonds' for the financial support enabling my stay in Potsdam. I would also like to thank Vincent Icke, for the helpful suggestions and discussions.

Appendix A: Finite elements solver

The GSE equation was solved by using the method of finite elements, which is suited to solve second-order partial differential equations like the GSE. The procedure was based on work on the special relativistic GSS originally introduced by Camenzind (1987), that was further developed by Haehnelt (1990), who included Kerr metrics. Fendt (1994, 1995, 1997) extended the code to get solutions extending throughout the outer light cylinder. More recently, Memola (2001) has worked on the special relativistic code including differential rotation of the field lines. For the purpose of this master-thesis, the code has been extended to include both the source term due to differential rotation of the field lines as well the Kerr metric.

In general, for problems that cannot be solved by Variational methods, a *Galerkin ansatz* of weighted Residues is used (see Schwarz 1984): The integration area G is discretized in a grid of finite elements with each element containing m knots. The function $\Psi(r,\theta)$ is approximated at each grid-element (e) by an expansion into m linearly-independent functions,

$$\Psi^{(e)}(r,\theta) = \sum_{i=1}^{m} c_i^{(e)} N_i^{(e)}(r,\theta) \tag{6.1}$$

where the the knot-variables $c_i^{(e)}$ are chosen such that they represent the function value $\Psi_i^{(e)}$.

The solution on the whole area can be represented by combining all the initial expansions of the individual grid elements,

$$\Psi(r,\theta) = \sum_{k=1}^{n} \Psi_k N_k^{(e)}(r,\theta) \tag{6.2}$$

where the summation now is over all n knot-points of the grid, and the set of global form-functions $N_k^{(e)}(r,\theta)$ are taken from the element-form-functions $N_i^{(e)}(r,\theta)$, that have the value of one in knot-point k.

With this Ansatz, the differential equation will only be fulfilled up to a Residual $\Re(r,\theta)$. The accuracy depends on the number of knots, or the number of expansion coefficients. The *Method of Galerkin* demands for minimizing the Residual, that the integral of the Residual, weighted with a specific weight-function W_j over the integration area, dissapears,

$$\iint_D \Re(r,\theta)\, W_j(r,\theta)\, dA = 0 \tag{6.3}$$

in case of the GSE the Residual is

$$\Re(r,\theta) = \tilde{\omega}\nabla\cdot\{\frac{\alpha D}{\tilde{\omega}^2}\nabla\left(\sum_{k=1}^{n}\Psi_k N_k(r,\theta)\right)\} - J \tag{6.4}$$

where J is the source-term of the GSE. If the m functions N_i are taken as the weight-function, a set of m linear independent equations remain for each grid element, that can be solved in principle to the coefficients Ψ_k. Then the solution $\Psi(r,\theta)$ is fully determined.

The integral can be done by using Green's Identity so that one retains the 'weak form' of the GSE,

$$\iint \frac{\alpha D}{\tilde{\omega}}\nabla N_i\cdot\nabla\Psi dA = \iint JN_i dA + \oint \frac{\alpha D}{\tilde{\omega}} N_i \frac{\partial\Psi}{\partial n} ds \tag{6.5}$$

This gives a matrix,

$$A_{ij} = \iint \frac{\alpha D}{\tilde{\omega}}\left(\Delta\partial_r N_i\partial_r N_j + \partial_\theta N_i\partial_\theta N_j\right)\frac{drd\theta}{\sqrt{\Delta}} \tag{6.6}$$

and a vector

$$B_i = \iint_{\partial D} N_i J\frac{\rho^2}{\sqrt{\Delta}} drd\theta + \oint \frac{D}{\tilde{\omega}} N_i\partial_n\Psi ds \tag{6.7}$$

For the set of Ψ_k the following equation holds,

$$A(\Psi)\,\Psi = B(\Psi) \tag{6.8}$$

Appendix B : Choosing the grid

A grid was used with 128x128 finite elements. Each of the isoparametric curvilinear finite element (Schwarz 1984; Cesari 1994) is formed of 8 grid points, or nodes, which gives a total of 49665 grid-points for the whole grid at which the GSE is discretized. For the inner solution from 128 elements in the z-direction, 27 grid points were used at the black hole ergosphere, and 24 grid points at the accretion disk.

The structure of the grid is shown in Fig. 6.1. For the inner grid shape of the left and right boundaries were specified. The elements were divided in steps of equal (dR, dZ) in both directions. A straight line then connected the left and the right elements in a straight line. For each line, the spacings of (dR, dZ) were equal.

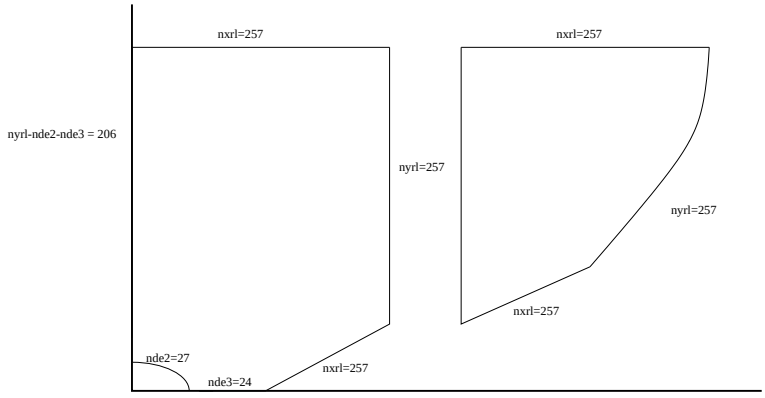

Figure 6.1: setup of grids chosen for inner and outer region

Bibliography

[1993a] Appl, S. & Camenzind, M. 1993, A&A, **270**, 71

[1993b] Appl, S. & Camenzind, M. 1993, A&A, **274**, 699

[1996] Appl, S. 1996, A&A, **314**, 995

[1997] Baade, W. & Minkowski, R. , 1954, ApJ, **119**, 215

[1993] Beskin V. S. & Pariev, V. I. 1993, Physics Uspekhi, **36**, 529

[1999] Biretta, J. A. , Sparks, W. B. & Macchetto, F. 1999, ApJ, **520**, 621

[2002] Biretta, J. A. , Junor, W. , Livio, M. 1999, NAR, **46**, 239

[1974] Blandford, R. D. & Rees, M. J. 1974, MNRAS, **169**, 395

[1977] Blandford, R. D. & Znajek, R. L. 1977, MNRAS, **179**, 433

[1982] Blandford, R. D. & Payne, D. G. 1982, MNRAS, **199**, 883

[1997] Bogovalov, S. 1997, A&A, **327**, 662

[1998] Boyer, R. H. & Lindquist R. W. 1967, J. Math. Phys. , **8**, 265

[1986] Camenzind, M. 1986, A&A, **162**, 32

[1987] Camenzind, M. 1987, A&A, **184**, 341

[2002] Casse, F. & Keppens, R. , ApJ, **581**, 988

[1993] Celotti, A. , Fabian, A. , C. 1993, MNRAS, **264**, 228

[1991] Chiueh T. , Li, Z. Y. & Begelman M. C. 1991, ApJ, **377**, 462

[1994] Contopoulos, J. & Lovelace, R. V. E. 1994, ApJ, **429**, 139

[1995] Contopoulos, J. 1995, ApJ, **446**, 67

[2000] Dhawan, V. , Mirabel, I. F. & Rodríguez, L. F. 2000, ApJ, **543**, 373

[1994] Fendt, C. 1994, PhD Thesis

[1995] Fendt, C. & Camenzind, M. 1995, A&A, **300**, 791

[1996] Fendt, C. & Camenzind, M. 1996, A&A, **313**, 519

[1997] Fendt, C. 1997, A&A, **319**, 1025

[1997] Fendt, C. 1997, A& A, **323**, 999

[2001] Fendt, C. & Memola E. 2001, A&A, **365**, 631

[2001] Fendt, C. & Greiner J. 2001, A&A, **369**, 308

[1937] Ferraro, V. C. A. 1937, MNRAS, **97**, 458

[1997] Ferreira, J. 1997, A&A, **319**, 340

[1994] Ford, R. J. , Harms, Z. I. et al. 1994, ApJ, **435**, L27

[2001] Greiner, J. , Cuby, J. G. , McCaughrean, M. J. 2001, Nature, **414**, 522

[1990] Haehnelt, M. 1990, Dipl.Thesis

[1998] Herrnstein, J. R. , Moran, J. M. et al. 1998, ApJ, **505**, 243

[1989] Heyvaerts, J. & Norman, C. A. , 1989, ApJ, **347**, 1055

[2003] Heyvaerts, J. & Norman, C. A. , 2003, astr0-ph/039128

[1989] Icke, V. 1989, A&A, **216**, 294

[1999] Junor, W. , Biretta, J. A. , Livio, M. 1999, Nature, **401**,891

[1992] Khanna, R. & Camenzind, M. 1992, A&A, **263**, 401

[1999] Krolik, J. H. 1999, *Active Galactic Nuclei*, Princeton Series in Astrophysics, 290

[1996] Kudoh, T. & Kaburaki, O. 1996, ApJ, **460**, 1999

[1998] Koide, S. , Shibata, K. & Kudoh, T. 1998, ApJ, **495**, L63

[2001] Komissarov, S. S. 2001, MNRAS, **326**, L41

[2000] Lery, T. , Frank, A. 2000, ApJ, **533**, 897

[1996] Lery, T. , Ph. D. thesis, ULP Strasbourg

[1992] Li, Z. Y. , Chiueh, T. & Begelman, M. C. 1992, ApJ, **394**, 459

[1993] Li, Z. Y. 1993, ApJ, **415**, 118

[1991] Lovelace, R. V. E. , Berk, H. L. & Contopoulos, J. 1991, ApJ, **379**, 696

[1991] Lovelace, R. V. E. , Romanova, M. M. & Contopoulos, J. 1993 ApJ, **403**, 158

[2001] Memola, E. 2001, Phd. Thesis, AIP Potsdam

[2002] Mészáros, P. 2002, ARA&A, **40**, 137

[1969] Michel, F. C. 1969, ApJ, **158**, 727

[1973] Michel, F. C. 1973, ApJ, **180**, 207

[1999] Mirabel, I. , F. & Rodriguez L. , F. 1999, ANRA&A, 37

[1995] Miyoshi, M. , Moran, J. et al. 1995, Nature, **373**, 127

[1983] Mundt, R. & Fried J. , W. 1983, ApJ, **274**, L83

[1998] Mundt, R. & Eislöffel J. , W. 1998, AJ, **116**, 860

[1991] Nitta, S. Takahashi, M. & Tomamitsu, A. 1991, Phys. Review D, **44**, 2295

[1992] Okamoto, I. 1992, MNRAS, **254**, 192

[1997] Okamoto, I. 1997, A&A, **326**, 1277

[1999] Okamoto, I. 1999, MNRAS, **307**, 253

[1999] Ouyed, R. & Pudritz, R. E. 1999, MNRAS, **309**, 233

[1997] Pariev, V. I. , Istomin, Ya. N. & Beresnyak, A. R. 2003, A&A, **403**, 805

[1992] Pelletier, G. , Pudritz, R. 1992, ApJ, **394**, 117

[1999] Perlman, E. S. , Biretta, J. A. et al. 1999, AJ, **117**, 2185

[2002] Perlman, E. S. , Biretta, J. A. et al. 2002, NAR, **46**, 399

[1987] Phinney, E. S. 1987, in *Superluminal Radio Sources*, eds. J. A. Zensus sand T. J. Pearson, 301

[2001] Punsly, B. 2001, *Black Hole Gravitohydromagnetics*, Springer Verlag, New York

[1996] Reynolds, C. S. , Fabian, A. C. , Celotti, A. & Rees, M. J. 1996, MNRAS, **283**, 873

[1985] Sakurai, N. I. 1985, A&A, **152**, 121

[1987] Sakurai, N. I. 1987, PASJ, **39**, 821

[1980] Stoer, J. & Boelirsch, R. 1980, *Introduction to Numerical Analysis*, Springer, New York

[1990] Takahashi, M. , Nitta, S. , et al. 1990, ApJ, **363**, 206

[1982] Thorne, K. S. & Macdonald, D. 1982, MNRAS, **198**, 339

[1995] Zensus, J. A. , Cohen, M. H. & Unwin, S. C. 1995, ApJ, **443**, 35